Experimental Study of the Heat Transfer on a Squealer Tip Transonic Turbine Blade with Purge Flow

James Phillips

Thesis submitted to the faculty of the
Virginia Polytechnic Institute and State University
in partial fulfillment of the requirements for the degree of

Master of Science
In
Mechanical Engineering

Wing F. Ng, Chair
Srinath V. Ekkad
Thomas E. Diller

December 9, 2013
Blacksburg, Virginia

Keywords: Squealer Tip, Experimental Heat Transfer, Purge Flow, Transonic

Experimental Study of the Heat Transfer on a Squealer Tip Transonic Turbine Blade with Purge Flow

James Phillips

Abstract

The objective of this work is to examine the flow structure and heat transfer distribution of a squealer tip rotor blade with purge flow cooling and provide a comparison with a basic flat tip rotor blade without purge flow cooling, under transonic conditions and high inlet freestream turbulence intensity. The blade design was provided by Solar Turbines Inc., and consists of a double squealer around the pressure and suction sides, two purge flow blowing holes located downstream of the leading edge and mid-chord, four ribs in the mid-chord region and a trailing edge bleeder exiting on the pressure side. Blade cavity depth is 2.29 mm (0.09 in.) and the total blade turning angle is 107.5°. Tests were performed in a blow-down facility at a turbulence intensity of 12%, in a seven bladed 2-D linear cascade at transonic conditions. Experiments were conducted at isentropic exit Mach numbers of 0.85 and 1.05, corresponding to Reynolds numbers based on axial chord of 9.75×10^5 and 1.15×10^6, respectively, and tip clearance gaps of 1% and 2% of the scaled engine blade span. A blowing ratio of 1.0 was used in the squealer tip experiments. Detailed heat transfer coefficient and film cooling effectiveness distributions were obtained using an infrared thermography technique, while oil flow visualization was used to investigate the flow patterns in the blade tip region.

With the addition of a squealer tip, leakage flow was found to decrease, as compared to a flat tip blade. With increasing tip clearance gap, the heat transfer coefficients within the cavity and along the squealer rim were found to decrease and increase, respectively. Film cooling effectiveness decreased with increasing tip clearance gap and was mainly observed within the squealer cavity. The maximum heat transfer coefficient was observed on the leading edge, however, comparatively large values were observed on the mid-chord ribs. The presence of the ribs, greatly affected the flow structure and heat transfer distributions within the cavity and downstream towards the trailing edge.

Acknowledgements

I would like to thank many people who have helped me through the unique challenges on my way to completing my Master's degree. Without the help of my professors, family members, department staff, friends and colleagues, I would truly not have been able to complete my degree.

Dr. Wing Ng's leadership and guidance through the rigorous subjects of heat transfer and turbomachinery were paramount to my successes thus far and I am extremely grateful to have had him as my advisor. Dr. Srinath Ekkad's support and initial guidance in the field of convection heat transfer piqued my interest in the subject. I would also like to thank Dr. Thomas Diller for raising tough questions about my research and working patiently with me though their resolution. The insights gained in Dr. Brian Vick's graduate courses prepared me to understand the complex analysis methods used in the various areas of my research. Without the help and expertise of Johnny, Bill and Philip of the Mechanical Machine Shop, I would not have completed the design and fabrication of my test components. I would also like to thank my contacts at Solar Turbines Inc., Dr. Hee-Koo Moon and Dr. Luzeng Zhang, for their support and sponsorship of this research.

The support of my friends and colleagues who helped both in and out of the tunnel is greatly appreciated. Dr. Song Xue's guidance and leadership from the beginning of my time in graduate school was of the utmost help. Without Dorian Blot's mastery of the tunnel run code, I would literally have not been able to conduct my research. My conversations with Arnab Roy about the data reduction method and many other technical topics led to various insights throughout my time as a researcher. Finally, I would like to thank my partner on the Solar Project, Allan Arisi, who has struggled with the complex problems inherent to our research along with me since the beginning. Without his help and unique insight, I would not be where I am today.

I would also like to thank my parents, Jim and Lisa Phillips, for their financial and emotional support throughout my undergraduate and graduate career. They were always there to encourage and motivate me to do my very best and not be afraid to fail. Without their support and the support of everyone else I've listed here, I would not have accomplished this milestone in my life, so thank you once again.

Table of Contents

Abstract ii

Acknowledgements iii

Table of Contents iv

List of Figures vi

List of Tables ix

Nomenclature x

Introduction 1

Literature Review 1

Experimental Setup 4

Data Reduction Technique 8

Results and Analysis 11

- Oil Flow Visualization Results 11
- Heat Transfer Results 15
- Comparison of Flat to Squealer Tip with Purge Flow Blowing 20

Conclusions 24

Acknowledgements 25

References 25

Appendix A: Cascade Setup 27

- ABS Tip of the Center Test Blade 27
- Stainless Steel Base of the Center Test Blade 27
- Fully Assembled Center Test Blade 28
- Mounting and Adjustment of Blade Tip Clearance in the Test Section 28

Appendix B: Tunnel Condition Calculation 30

- Downstream Static Pressure Tap Layout 30
- Static Pressure Measurement Technique 30
- Blowing Ratio Measurement Technique 31
- Blade Passage Periodicity 32

Typical Temperature Distributions 33
Appendix C: Infrared Technique 35
Linear Regression Data Reduction 35
Recovery Temperature Calculation 37
Near Purge Hole Effect on Wall Temperature 39
Appendix D: Additional Results 41
Oil Flow Visualization Results 41
Heat Transfer Results 44
NO PURGE FLOW BLOWING, BLOWING RATIO = 0 44
PURGE FLOW BLOWING, BLOWING RATIO = 1.0 47
COMPARISON OF FLAT AND SQUEALER TIP RESULTS 52
Conclusions 54
Appendix E: Accuracy of Finite-Difference Code 56
Appendix F: Material Properties Correction 58
Appendix G: Uncertainty Analysis 59
Appendix H: Appendix References 61

List of Figures

Figure 1. Scale model of the Transonic Wind Tunnel at Virginia Tech 4
Figure 2. Linear cascade with three squealer tip blades, capable of purge flow blowing, and four support blades without tip clearance gaps 5
Figure 3. Tip and internal geometry of the test blade 7
Figure 4. Flat tip flow visualization results at an exit Mach number of 0.85 and tip clearance gaps of (a) 1% and (b) 2%, as reported by Anto et al. [9] 12
Figure 5. Flat tip suction side flow visualization results at an exit Mach number of 0.85 and tip clearance gaps of (a) 1% and (b) 2%, as reported by Anto et al. [9] 13
Figure 6. Squealer tip flow visualization results at an exit Mach number of 0.85, a blowing ratio of 1.0 and tip clearance gaps of (a) 1% and (b) 2% 14
Figure 7. Squealer tip endwall flow visualization results at an exit Mach number of 0.85, a blowing ratio of 1.0 and tip clearance gaps of (a) 1% and (b) 2% 15
Figure 8. Squealer tip suction side flow visualization results at an exit Mach number of 0.85, a blowing ratio of 1.0 and tip clearance gaps of (a) 1% and (b) 2% 15
Figure 9. Flat tip heat transfer coefficient results at an exit Mach number of 0.85 and tip clearance gaps of (a) 1% and (b) 2% 16
Figure 10. Squealer tip heat transfer coefficient results at an exit Mach number of 0.85, a blowing ratio of 1.0 and tip clearance gaps of (a) 1% and (b) 2% 18
Figure 11. Squealer tip film cooling effectiveness results at an exit Mach number of 0.85, a blowing ratio of 1.0 and tip clearance gaps of (a) 1% and (b) 2% 18
Figure 12. Regions for averaged circumferential results, corresponding to Figures 13 and 14 .. 21
Figure 13. Circumferential averaged heat transfer coefficient and film cooling effectiveness results by region for flat and squealer tip blades at an exit Mach number of 0.85 and a tip clearance gap of 1% 22
Figure 14. Circumferential averaged heat transfer coefficient and film cooling effectiveness results by region for flat and squealer tip blades at an exit Mach number of 0.85 and a tip clearance gap of 2% 23
Figure 15. ABS tip of the test blade 27
Figure 16. Stainless steel base of the test blade 27
Figure 17. Squealer tip blade with purge flow cooling supply and plenum pressure tap 28

Figure 18. Tip gap adjustment hardware 29
Figure 19. Test section with squealer tip blades installed 29
Figure 20. Endwall pressure tap locations in relation to blade geometry 30
Figure 21. Average local exit Mach number for six downstream static pressure ports and all tunnel runs 33
Figure 22. Typical temperature distribution at a single point on the blade surface for two tunnel runs at two different temperature coolants 34
Figure 23. CAD drawing of IR window installed in the test section 35
Figure 24. Linear regression fit for the first method of calculating recovery temperature 38
Figure 25. Linear regression progression for the second method of calculating recovery temperature 39
Figure 26. Wall temperature plots for an entire tunnel run at near purge hole and away from purge hole points at tip clearance gaps of 1% and a Mach number of 0.85 40
Figure 27. Flat tip oil flow visualization for an exit Mach number of 0.85 and tip clearance gaps of (a) 1% and (b) 2%, as reported by Anto et al. [H-4] 41
Figure 28. Flat tip suction side oil flow visualization for an exit Mach number of 0.85 and tip clearance gaps of (a) 1% and (b) 2%, as reported by Anto et al. [H-4] 41
Figure 29. Squealer tip oil flow visualization for Mach numbers of 0.85 and 1.05 and tip clearance gaps of 1% and 2%, at a BR=1.0 42
Figure 30. Squealer tip suction side oil flow visualization for Mach numbers of 0.85 and 1.05 and tip clearance gaps of 1% and 2% at a BR=1.0 42
Figure 31. Squealer tip endwall oil flow visualization for Mach numbers of 0.85 and 1.05 and tip clearance gaps of 1% and 2% 43
Figure 32. Heat transfer coefficient distributions of a flat tip blade of the same outer geometry as squealer tip blade of current study at different exit Mach numbers and tip clearance gaps 45
Figure 33. Heat transfer coefficient distributions of the squealer tip turbine blade at different exit Mach numbers and tip clearance gaps for a blowing ratio of 0 45
Figure 34. Heat transfer coefficient distributions of the squealer tip turbine blade at different exit Mach numbers and tip clearance gaps for a blowing ratio of 1.0 48
Figure 35. Film cooling effectiveness distributions of the squealer tip turbine blade at different exit Mach numbers and tip clearance gaps for a blowing ratio of 1.0 49

Figure 36. Net heat flux reduction distributions of the squealer tip turbine blade at different exit Mach numbers and tip clearance gaps 51
Figure 37. Circumferential averaged heat transfer coefficient and film cooling effectiveness results by region for flat and squealer tip blades at an exit Mach number of 1.05 and a tip clearance gap of 1% 53
Figure 38. Circumferential averaged heat transfer coefficient and film cooling effectiveness results by region for flat and squealer tip blades at an exit Mach number of 1.05 and a tip clearance gap of 2% 54
Figure 39. Temperature profile input into finite-difference code and Cook and Felderman equation 56
Figure 40. Output of finite-difference code and Cook and Felderman analytical solution 57
Figure 41. Correlation between a percent increase in the material property values and a percent increase in the heat transfer coefficient and film cooling effectiveness results presented in this study 58

List of Tables

Table 1. Calculation of the precision, bias and total uncertainty within the heat transfer coefficient measurements..... 59
Table 2. Calculation of the precision, bias and total uncertainty within the film cooling effectiveness measurements..... 60

Nomenclature

BR	Averaged blowing ratio ($=\rho_c U_c/\rho_\infty U_{\infty,avg}$)
C	True chord of blade (69.9 mm, 2.75 in.)
C_p	Constant pressure specific heat
C_x	Axial chord of blade (58.2 mm, 2.29 in.)
h	Local heat transfer coefficient
k	Thermal conductivity
Ma	Mach number
P	Pressure
q”	Heat flux
Re	Reynolds number
T	Temperature
TG	Tip Clearance Gap (% of engine blade span)
U	Velocity

Greek Symbols

γ	Specific heat ratio of air
η	Local film cooling effectiveness
μ	Dynamic viscosity of air
ρ	Local density of air
ϕ	Overall film cooling effectiveness

Subscripts

0	No purge flow blowing
1	Inlet conditions
2	Exit conditions
c	Coolant
i	Initial conditions
o	Stagnation or total
r	Recovery
w	Wall
∞	Mainstream

Introduction

In modern gas turbine engines, air is pressurized in a compressor, mixed with fuel and ignited in a combustor. The combustion products then enter the turbine where the mechanical rotation of the rotor can be used for many power generation applications. Increasing the combustion temperature and subsequently the turbine inlet temperature, leads to an improvement in the overall efficiency of the gas turbine engine. While this increase in efficiency is desirable, the increased temperature of the gas entering the turbine section can cause degradation and mechanical failure of the turbine components. Bunker [1] reports that approximately one third of high pressure turbine failures occur due to blade tip degradation. Leakage flow over the tip of an unshrouded turbine blade is the cause of both mechanical failure and decreased efficiency. These deficiencies are exacerbated due to the transonic conditions present in the three-dimensional flow over the turbine tip [2]. Blade tip experimental and numerical research is invaluable to understanding of the complex fluid flows and heat transfer distributions present in modern gas turbine engines.

Literature Review

The effect tip gap has on the flow field has been studied by Sjolander and Cao [3] for a simplified flat tip blade geometry within a stationary linear cascade. Using flow visualization and chord-wise pressure measurements, they found that the flow over the tip of the blade separates at the pressure side edge and can reattach further down the flow path on the surface of the tip. This reattaching flow impinges on the surface of the tip and fluid flows towards both the pressure and suction sides. The impinged flow heading towards the pressure side produces a counter-rotating vortex when it interacts with the leakage flow over the pressure side. This counter-rotating fluid region near the pressure side is therefore expected to have a large heat transfer coefficient.

Kwak et al. [4] conducted a similar study on a GE-E^3 turbine blade with single and double squealer tips and rims located on the pressure side, suction side or camber line. Common to all cases was the separation region at the pressure side of the blade; however, the location of the squealer rim significantly affected the reattachment location. Recirculation regions develop as a result of the squealer rim, which are larger than those produced by a flat tip blade. Kwak et al. [4] determined that changing the squealer rim location changes the leakage flow path which in

turn produces different heat transfer distributions across the tip and that a squealer rim located on the suction side of the blade would produce the lowest heat transfer coefficient on the blade tip. Azad et al. [5] came to the same conclusions as Kwak et al. [4] in a similar experiment and in both cases it was found that the use of a squealer rim significantly reduces the amount of leakage flow over the blade tip as compared to a flat tip blade. Bunker [1] predicts a linear relationship between tip clearance and stage efficiency loss and that a 1% tip gap for flat and squealer tip blades will reduce the stage efficiency by 2% and 1.5%, respectfully.

Mayle and Metzger [6] showed in an early study that the heat transfer coefficient on the blade tip is basically independent of the relative motion between the tip and its stationary wall. The difference in heat transfer coefficient between rotating and non-rotating experiments was found to be within the experimental uncertainty of $\pm 10\%$, by the methods of Kline and McKlintock [7]. This conclusion has led to the belief that the pressure difference between the pressure and suction sides of the blade is the dominating factor in regard to tip leakage flow. Thus stationary configurations have become the most popular method of performing experimental measurements on turbomachinery components. Yang et al. [8] have more recently conducted a numerical simulation where the effect of the relative rotation of the blade and endwall on the heat transfer coefficient, for flat and squealer tip GE-E^3 first stage turbine blades, was investigated. For both flat and squealer tip blades, the relative motion of the endwall decreased the leakage flow over the tip and significantly increased the heat transfer coefficient. The high heat transfer regions for the nonrotating and rotating cases are located at the leading edge on the suction side of the cavity and the pressure side of the cavity, respectively.

Anto et al. [9] conducted heat transfer experiments on a flat tip blade of the same geometry, experimental setup and test conditions as in the current study, isentropic exit Mach numbers of 0.85 and 1.05 and tip clearance gaps of 1% and 2% of the scaled engine blade span. He found that the heat transfer coefficient increased with increasing Mach number and tip gap. Furthermore, an increase in the Mach number, from 0.85 to 1.05, produces a larger heat transfer coefficient increase than an increase in the tip gap, from 1% to 2%.

Zhang et al. [10] conducted a similar study to Anto et al. [9] where the flat tip heat transfer distribution, at Mach and Reynolds numbers of 1.0 and 1.27×10^6, respectively, was examined experimentally and numerically. They reported that an increasing tip gap corresponds to an increase in tip gap Mach number as well as an increase and decrease of the Nusselt number

in the leading edge and trailing edge regions, respectively. Subsonic flow was reported in the leading edge region coinciding with the largest Nusselt numbers. Supersonic flow was observed across most of the tip towards the trailing edge and coincides with low Nusselt number region. A multiple oblique shock structure was observed in the mid-chord to trailing edge region producing striped pattern on the heat transfer distribution.

Kwak et al. [4] showed, in the experiment previously mentioned, that the heat transfer coefficient on the blade tip and endwall were significantly reduced by the use of a squealer tip as opposed to a flat tip blade. Their test conditions included tip gaps of 1.0%, 1.5% and 2.5% of blade span, Reynolds number of 1.1×10^6, turbulence intensity at the cascade inlet of 9.7%, pressure ratio of 1.2 and exit Mach numbers of 0.25 and 0.59 in a five bladed linear cascade blow down facility. Using the same blade geometry and test conditions, Kwak et al. [11] added film cooling holes along the camber line to both flat and squealer tip blades. They found that the overall heat transfer coefficient increased with increasing tip gap and decreased with increasing blowing ratio, while the film cooling effectiveness increased with increasing blowing ratio. Also, the film cooling effectiveness increased and heat transfer coefficient decreased when comparing the squealer to the flat tip blades.

Ameri et al. [12] conducted a numerical study on the flow and heat transfer of flat and squealer tip GE-E^3 first stage turbine blades. They found that when compared to a flat tip blade the heat transfer coefficient within the cavity of a squealer tip blade was higher. The heat transfer coefficient on the pressure side rim of the squealer tip was comparable to the flat tip blade but the suction side rim was higher. The high heat transfer coefficient regions in the cavity of the squealer tip are due to the reattaching mainstream flow and the heat transfer coefficient levels in the cavity are less than those observed on the squealer rim. Kwak et al. [11] saw that the heat transfer coefficient on the rim does not change appreciably for different blowing ratios and that it is higher than the heat transfer coefficient in the cavity, except for immediately behind the leading edge. They also observed that near the leading edge, where the blade is wider, clear reattachment and recirculation regions are present. Towards the trailing edge, where the blade is narrower, a reattachment region is not observed. Kwak et al. [11] attributes the lack of the reattachment region to the blade geometry and the low heat transfer coefficient levels observed as a result of a recirculation of coolant.

As evidenced in the preceding section, many studies have been conducted, both experimental and numerical, on the tip region of turbine blades. However, most of these studies have been conducted at lower speeds and turbulence intensities than would be observed in a modern turbine. Due to the complex nature of the flow and the presence of comparable flat tip results, an examination of heat transfer distributions at various tip clearance gaps at high speed conditions will provide many insights into tip heat transfer on turbine blade surfaces.

Experimental Setup

The current study was conducted at Virginia Tech's Transonic Wind Tunnel, which is a blow down facility capable of producing isentropic exit Mach numbers above 1.0. This facility has been used in previous heat transfer experiments by Anto [9], Holmberg [13], Nix et al. [14], Smith et al. [15], Popp et al. [16], Carullo et al. [17] and Nasir et al. [18]. Figure 1 shows a scale drawing of the wind tunnel as seen in the test facility.

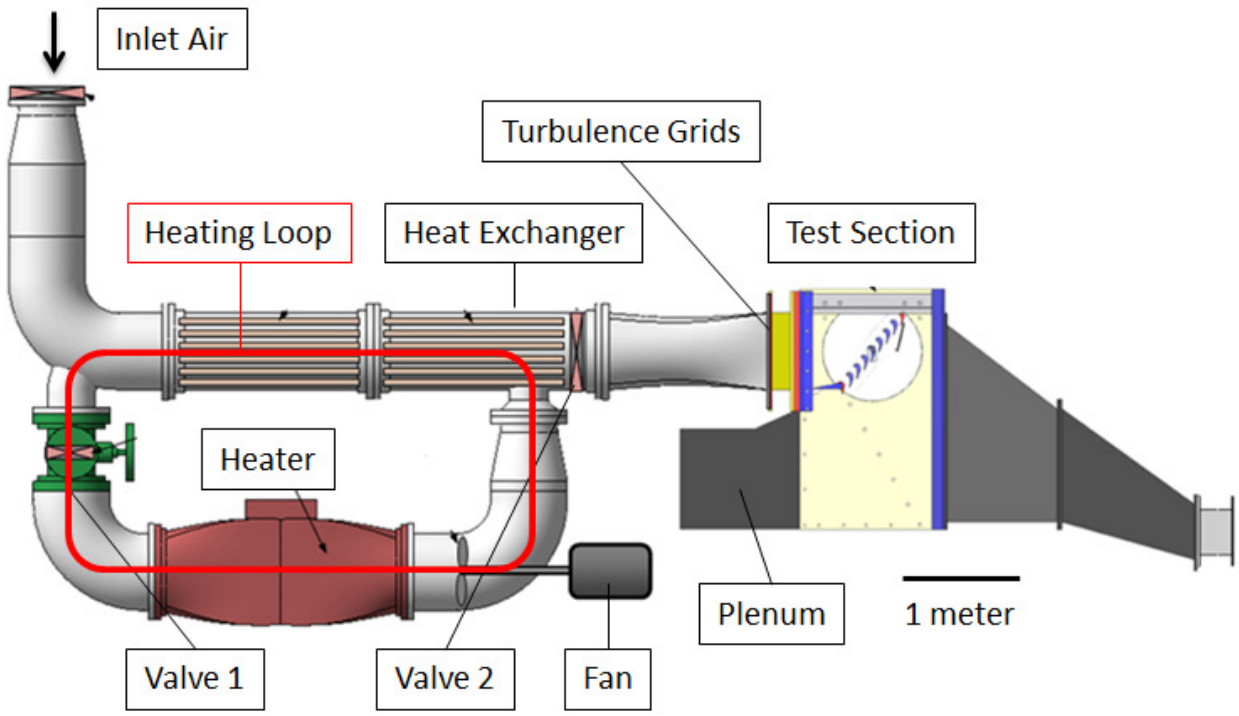

Figure 1. Scale model of the Transonic Wind Tunnel at Virginia Tech

An upstream compressor can safely pressurize air up to 1725 kPa (250 psig) in a high volume storage tank. A main control valve is located upstream of the tunnel section pictured in Figure 1 and can hold a steady inlet pressure for up to 20 seconds, depending on the desired tank

and inlet pressure. Before a heat transfer run is started, valve 1 and valve 2 are closed and the heater and fan are turned on. When air within the heating loop reaches 115°C (240°F) the valves are opened and pressurized air is allowed through the heat exchanger. Before entering the test section, the mainstream flow passes through a turbulence grid of 48% solidity, which produces a free-stream turbulence intensity of 12%. The turbulence grid has had hot-film anemometry measurements conducted on it by Nasir et al. [18] to measure the turbulence intensity. Once through the turbulence grid, the mainstream flow enters the test section shown in Figure 2. A downstream plenum is used to decrease the effect of flow blockage associated with a high-turning angle blade.

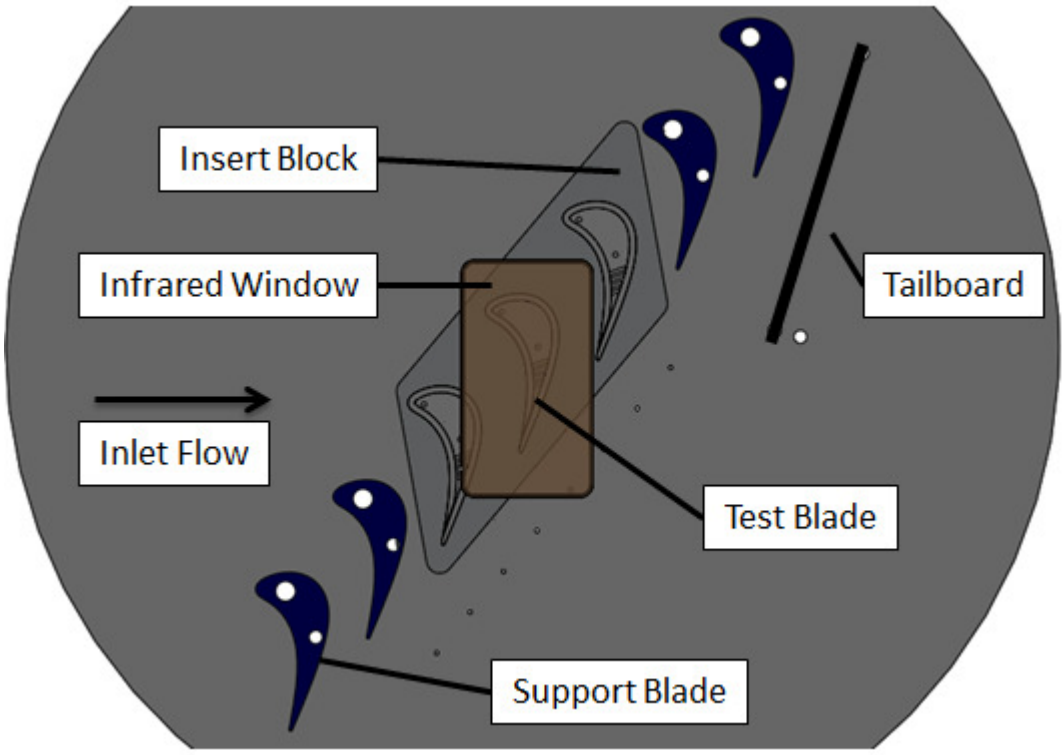

Figure 2. Linear cascade with three squealer tip blades, capable of purge flow blowing, and four support blades without tip clearance gaps

The test section consists of seven full blades, three of which are either flat or squealer tip blades equipped for purge flow blowing, four are support blades which help hold the test section together and do not have tip clearance gaps, also there are two half blades (not pictured) at the top and bottom of the cascade. The test section blades have a pitch of 5.82 cm (2.29 in.), a span of 15.24 cm (6 in.) and a turning angle of 107.5°. True and axial chord values are 6.99 cm (2.75 in.) and 5.82 cm (2.29 in.), respectively. A Pitot-static tube is located 2.2 C downstream of the

turbulence grid, while the test blade is located 5.1 C downstream. The Pitot-static tube is used to calculate the inlet Mach number of the cascade. The static pressure ports located 0.5 C downstream of the blades, are used to calculate the isentropic exit Mach number. An insert block, which has the three test blades attached allows for the variation of tip clearance size. Flow and heat transfer distribution is investigated at two isentropic exit Mach numbers, 0.85 and 1.05, and two tip clearance gaps, 1% and 2% of the scaled engine blade span of 7.62 cm (3 in). The exit flow Reynolds number and Mach number are coupled in this test setup. Reynolds numbers of 9.75×10^5 and 1.15×10^6 are correspond with the exit Mach numbers of 0.85 and 1.05, respectively, and are based on the blade's axial chord. In Figure 2, overlaying the test blade is a Zinc Selenide, ZnSe, infrared camera window which is flush with the inside of the test section. A fixed tailboard is positioned downstream of the cascade to assist in producing periodic flow. Periodicity analysis of a similar cascade with the same blade geometry has been conducted by Carullo et al. [17]. Exit Mach number values at each of the downstream static pressure ports show a uniform trend and suggest that flow periodicity within the cascade is maintained. Figure 3 shows the tip geometry, along with the internal structure of the blade.

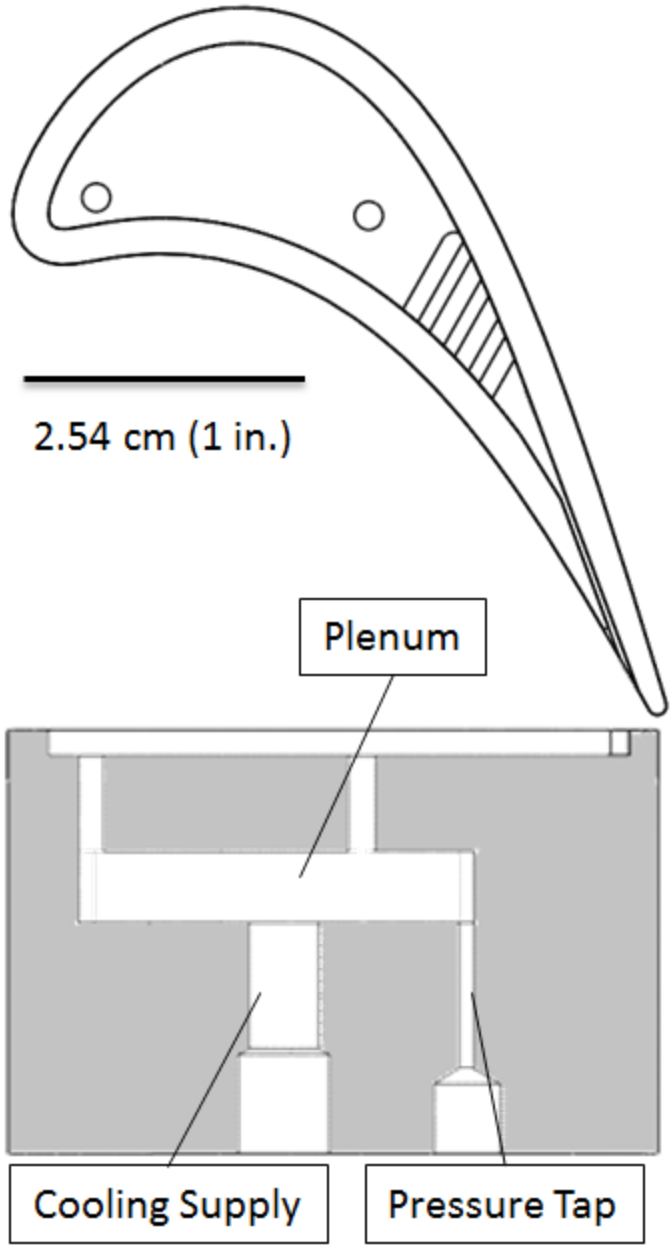

Figure 3. Tip and internal geometry of the test blade

The blade tip was printed in the Fortus 250mc three-dimensional printing machine by Stratasys using ABS P-430 material with a thermal conductivity of 0.188 W/mK. The test blade consists of a double squealer along the pressure and suction sides with a cavity depth of 2.29 mm (0.09 in.), two purge flow blowing holes with a diameter of 2.54 mm (0.1 in.), four support ribs and a bleeder opening on the pressure side of the blade. The two purge flow blowing holes are supplied with cooling air that accumulates in a plenum before entering the tunnel. A static pressure tap and Type-T thermocouple are located inside all three squealer tip blades to measure

purge flow conditions. The difference in plenum pressure and temperature between the three squealer tip blades is never more than 3%, therefore the purge flow exiting all three blades is approximately the same. A heat exchanger, which uses liquid nitrogen, is used to chill the coolant supply air, before it's supplied to the plenum, during the appropriate tunnel runs. Two solenoid valves are located in between the test section and heat exchanger to control bleeder air flow into the atmosphere and coolant flow into the test section. The solenoid valves are set to switch and allow coolant air into the test section just before mainstream flow reaches the test blades.

Data Reduction Technique

A linear regression technique is used to calculate the heat transfer coefficient and film cooling effectiveness across the surface of the blade tip. Using Newton's Law of Cooling, the convective heat flux, q''_w, is defined as in Equation 1, where T is the temperature of the fluid interacting with the wall, T_w is the wall temperature and h is the local heat transfer coefficient. For no purge flow blowing cases, the fluid temperature interacting with the wall is the recovery temperature, T_r, which is an adjusted value of the mainstream total temperature to account for friction heating due to transonic conditions. Equation 1 is used as the linear regression equation for the flat tip cases. For cases with purge flow blowing, the fluid temperature interacting with the wall is the film temperature, defined in Equation 2 with the film cooling effectiveness, η, where T_c is the coolant temperature. Combining Equations 1 and 2 produces Equation 3, the linear regression equation used to calculate the local heat transfer coefficient and film cooling effectiveness. The tunnel takes three seconds to ramp up to the desired given Mach number; the data taken within the next two seconds is used in the linear regression equation to provide results at a constant exit Mach number.

$$q''_w = h(T - T_w) \tag{1}$$

$$\eta = \frac{T_f - T_r}{T_c - T_r} \rightarrow T_f = \eta T_c + (1 - \eta) T_r \tag{2}$$

$$\frac{q''_w}{T_r - T_c} = h\frac{T_r - T_w}{T_r - T_c} - h\eta \tag{3}$$

The wall temperature, T_w, was measured with a calibrated FLIR A325 infrared camera at a frequency of 10 Hz. Coolant temperature, T_c, is measured inside the blade plenum with a Type-T thermocouple. The recovery temperature, T_r, is calculated using Equation 4, where r_c is the local recovery factor, Ma is the local Mach number, γ is the specific heat ratio of air and $T_{o,\infty}$ is the mainstream total temperature. The term in parenthesis, represented as C_r, is not known at every location along the blade tip surface. Observing that C_r and as a result the recovery temperature are independent of coolant temperature, a method of calculating C_r using two tunnel runs, at the same exit Mach number and tip clearance gap, and at different coolant temperatures is presented.

$$T_r = T_{o,\infty}\left(\frac{1 + r_c\frac{\gamma-1}{2}Ma^2}{1+\frac{\gamma-1}{2}Ma^2}\right) = T_{o,\infty}C_r \tag{4}$$

The recovery temperature is independent of cooling temperature and therefore the resulting linear regression plots for both tunnel runs should lie along the same line. Within the data reduction code, C_r is calculated using an iterative method to maximize the coefficient of determination, R^2, between the two sets of cooling data and provide the most linear fit to the linear regression equation. The coefficient of determination is a value between 0 and 1and is a measure of how well a set of data follows a linear trend, where a value of 1 is perfectly linear.

It is believed that errors have occurred within the measurement of the wall surface temperature due to the proximity of the blade tip to the infrared window. This close proximity results in large local heating, in a highly transient environment, of the infrared window that was designed for steady state applications. The use of the mainstream total temperature, $T_{o,\infty}$, within Equation 4 results in an under-prediction of the recovery temperature. Equation 5 below shows the correlation between the difference in total and recovery temperatures as related to the local Mach number, where r_c is the recovery factor estimated at 0.9, C_p is the specific heat of air and R is the specific gas constant for air. Using Equation 5, it is found that the local Mach number is highly over-predicted, due to the large difference in the total and recovery temperatures. To mitigate these non-realistic local Mach numbers a boundary layer correction is applied to the mainstream total temperature, resulting in a lower driving temperature. While this boundary layer total temperature provides more reasonable local Mach numbers, the heat transfer coefficient values observed are well above what is expected and what has been seen in literature.

It is therefore believed that errors produced due the nature of the experiment, close proximity of the infrared window and blade tip and incorrect total temperature, result in the disconnect between local Mach number and temperature difference. The method for calculating the recovery temperature in Equation 4 should be examined further. While the scale of the heat transfer coefficient results is in question the trends observed between different test cases are independent of the temperature difference and total temperatures used, therefore the comparisons reported in this study are unaffected. Film cooling effectiveness is relatively unaffected by changes in the temperature difference and total temperatures used.

$$Ma^2 = \frac{2\,C_p\left(T_{o,\infty} - T_r\right)}{(1 - r_c)\sqrt{\gamma R T_{o,\infty}}} \tag{5}$$

The final unknown term in the linear regression equation is the convective heat flux, q''_w. The heat flux is calculated using a finite-difference method which assumes semi-infinite and one-dimensional conduction. Cress [19] developed the finite-difference code which has been used by Nasir et al. [18], Xue [20] and most recently Anto et al .[9]. The energy equation, initial and boundary conditions correspond with Equations 5, 6, 7 and 8, respectively.

$$\frac{\partial T}{\partial t} = \alpha \frac{\partial^2 T}{\partial x^2} \tag{6}$$

$$T = T_i \; at \; t = 0 \tag{7}$$

$$q''_w(t) = -k \frac{dT}{dx} \; at \; x = 0 \tag{8}$$

$$q''_w(t) = -k \frac{dT}{dx} \; at \; x = 0 \tag{9}$$

The finite-difference code used has been checked against Equation 9, derived by Cook and Felderman [21] for constant material properties, measured surface temperatures and constant time sampling. The finite-difference code produces a heat flux that is less than 0.5% different than the Cook and Felderman equation. The finite-difference code was developed and is used for its ability to model multiple materials with variable properties and allow investigation into the validity of the semi-infinite assumption. Computation time of the finite-difference code is also not significant enough to necessitate the use of the Cook and Felderman equation.

$$q''(t_n) = \frac{2\sqrt{k\rho C_p}}{\sqrt{\pi\,\Delta t}} \sum_{j=1}^{n} \frac{T_j - T_{j-1}}{\sqrt{n-j} + \sqrt{n+1-j}} \tag{10}$$

The uncertainty of this study was calculated using the perturbation procedure described by Moffat [22] where the bias and precision errors are taken into account. Bias error is the uncertainty associated with the measurement setup and is caused by calibration, material property and data acquisition errors. Precision error is the uncertainty of reproducing a given experiment exactly and is caused by random error and unsteadiness. The overall uncertainty in the heat transfer coefficient and film cooling effectiveness results are $\pm$14.14% and $\pm$0.102, respectively. The assumption of one-dimensional conduction breaks down around the edges of the blade and around the purge holes; therefore the uncertainty will be higher in these regions. Also, a perturbation analysis of the uncertainty with regard to the measured wall temperature was conducted in an effort to quantify the effect of an incorrect temperature measurement. A wall temperature uncertainty of $\pm$10°C corresponds with an increase in the total uncertainty to $\pm$21.64% and $\pm$0.159 for heat transfer coefficient and film cooling effectiveness, respectively.

Results and Analysis

The following section describes the flow visualization and heat transfer results for the flat and squealer tip blades. When the blade tips are presented they are oriented as they are in the test section, where flow is horizontal from the left to the right of the page. The design condition at an exit Mach number of 0.85 and tip clearance gap of 1% is compared for the flat and squealer tip results, along with the off-design condition at an exit Mach number of 0.85 and tip clearance gap of 2%.

Oil Flow Visualization Results

Anto et al. [9] presented the following flat tip oil flow visualization results for a similar blade as that used in this study. Green, red and yellow pigments were applied to the flat tip blade on the tip, pressure and suction sides, respectively. Figure 4 presents the tip flow visualization results at a Mach number of 0.85 and tip clearance gaps of 1% and 2%. The green region indicates a low shear area where leakage flow is at a minimum. In the mid-chord region a large shear area is present as evidenced by the light coating of pressure side pigment. Pooled pigment along the pressure side suggests flow separation and a reduced shear region. Towards the

trailing edge, reattachment regions are visible where pigment has been dispersed. Comparing Figures 4a and 4b, there appears to be a greater dispersion of pigment which suggests more leakage flow over the tip with 2% tip clearance gap case.

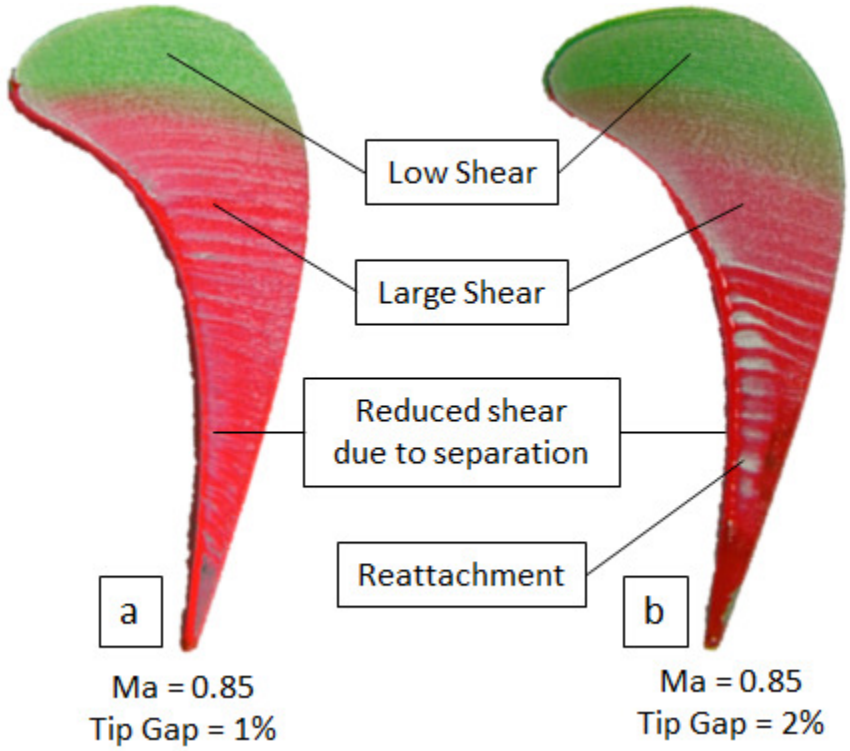

Figure 4. Flat tip flow visualization results at an exit Mach number of 0.85 and tip clearance gaps of (a) 1% and (b) 2%, as reported by Anto et al. [9]

Figure 5 presents the flat tip suction side flow visualization results at an exit Mach number of 0.85 and tip clearance gaps of 1% and 2%. As reported by Anto et al [9], the liftoff line for the design condition, where all three flow visualization pigments meet, is located about 0.13 inches (4.3% of the engine blade span) from the tip. From this metric, we estimate the impingement line to be located 0.585 inches (19.5% of the engine blade span) from the tip. The impingement line is not observed for the 2% tip clearance gap case and suggests that the leakage vortex is more detached from the suction side as compared to the 1% case, possibly due to the increased leakage flow over the tip.

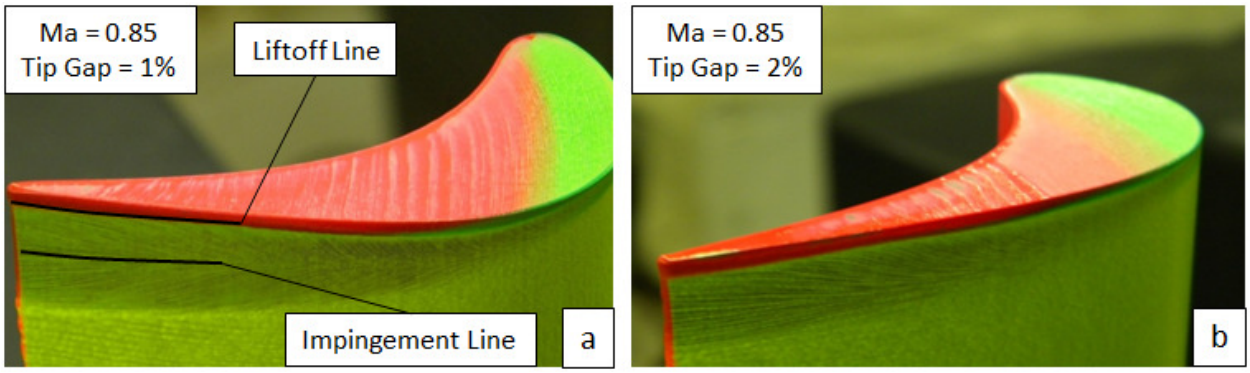

Figure 5. Flat tip suction side flow visualization results at an exit Mach number of 0.85 and tip clearance gaps of (a) 1% and (b) 2%, as reported by Anto et al. [9]

Figures 6 and 7 present the squealer tip and endwall flow visualization results at an exit Mach number of 0.85, a blowing ratio of 1.0 and tip clearance gaps of 1% and 2%. Yellow, blue, red, green and pink pigments were applied to the squealer pressure side, tip rim, tip cavity, suction side and endwall, respectively. Two reattachment regions appear in the cavity to the right of the leading edge, Figure 6a-ii. Impinging flow occurs where the mainstream flow reattached and is dispersed outward from the reattachment location.

In between the two reattachment regions where both impinging flows meet, cavity pigment is pooled, suggesting the presence of a liftoff region, Figure 6a-v. Present in the endwall flow visualization results, Figure 7a-ii, is a divergence of the pigment in the area immediately over the liftoff region, suggesting its effect is significant. Above the suction side rim a large separation bubble has formed causing flow blockage, as evidenced in the tip and endwall flow visualizations in Figures 6a-iv and 7a-i. Leakage flow is diverted around the separation bubble which causes cavity pigment to be deposited on the suction side rim.

Downstream of the leading edge, a recirculation region is present where reattaching mainstream flow is directed back towards the pressure side, Figure 6a-ii. Cavity flow travels downstream along the pressure and suction side rims. The suction side flow is turned by the support ribs and is directed upstream where a mixing region is evidenced by the pooling of cavity pigment, as shown in the tip and endwall flow visualizations, Figures 6a-iii and 7a-iii.

An increase in the tip clearance gap results in a downstream shift of the flow features as well as a lessening in their magnitude. Pressure side pigment also has a significant presence in the 1% tip clearance gap case in the trailing edge portion of the blade. This may be caused by the decreased flow speed over the tip as compared to the 2% case, where pressure side pigment

has a greater chance to reattach on the tip. Cavity pigment is present on the pressure side rim of the 2% tip clearance gap case due to the proximity of the downstream reattachment region with the pressure side and mid-chord purge hole.

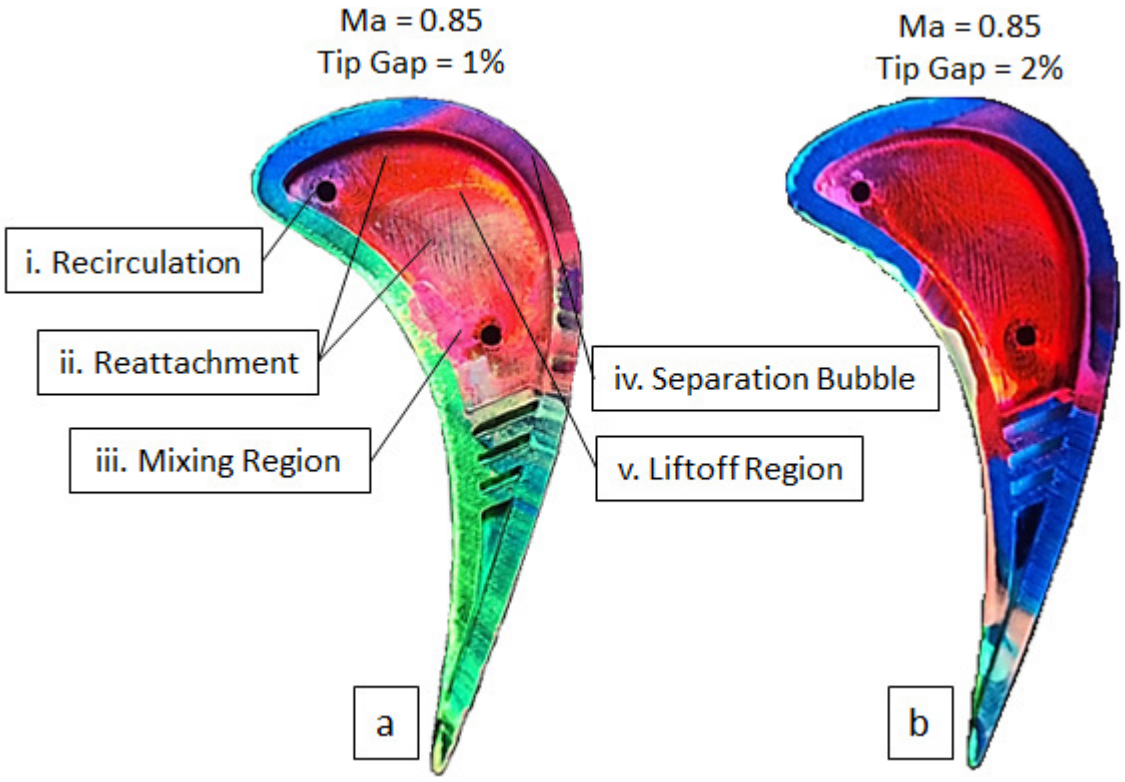

Figure 6. Squealer tip flow visualization results at an exit Mach number of 0.85, a blowing ratio of 1.0 and tip clearance gaps of (a) 1% and (b) 2%

Figure 8 presents the suction side squealer tip flow visualization results at an exit Mach number of 0.85, a blowing ratio of 1.0 and tip clearance gaps of 1% and 2%. In the 1% tip clearance gap case, the impingement line is located at 0.469 inches (15.6% of the scaled engine blade span). There appears to be a significant effect from the cavity flow on the suction side of the 1% tip clearance gap case as compared to the 2% case. The impingement line of the 2% case is almost non-existent, suggesting increased leakage flow over the tip.

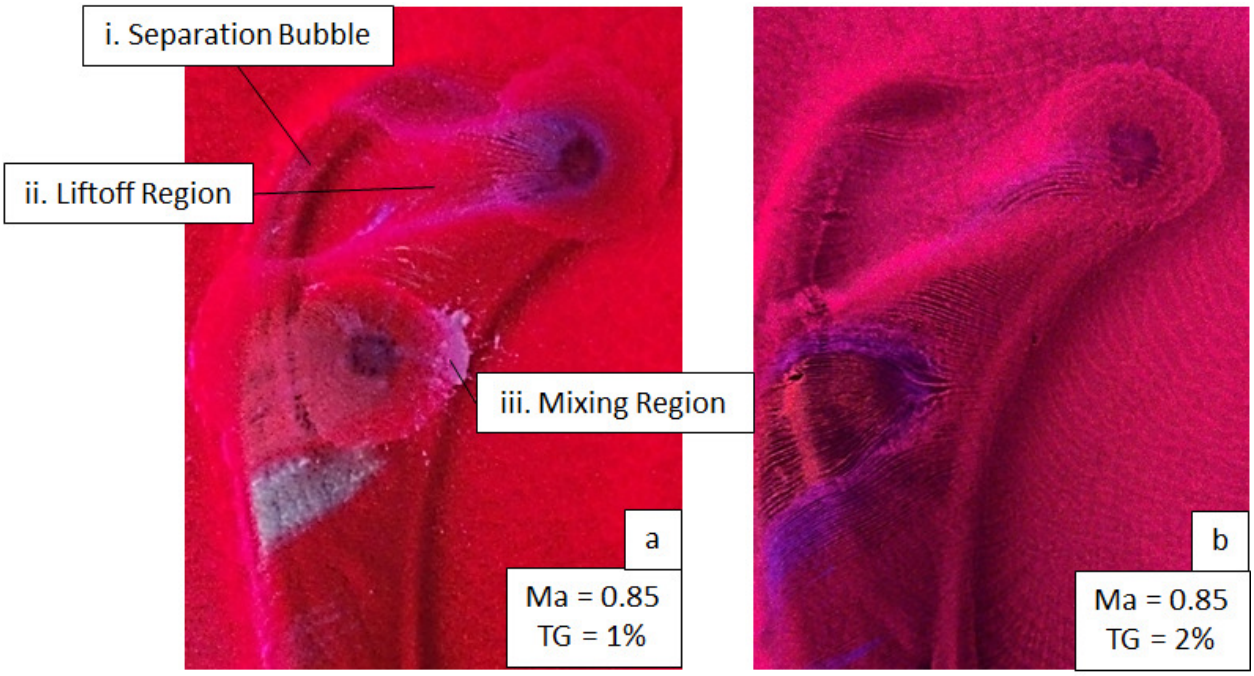

Figure 7. Squealer tip endwall flow visualization results at an exit Mach number of 0.85, a blowing ratio of 1.0 and tip clearance gaps of (a) 1% and (b) 2%

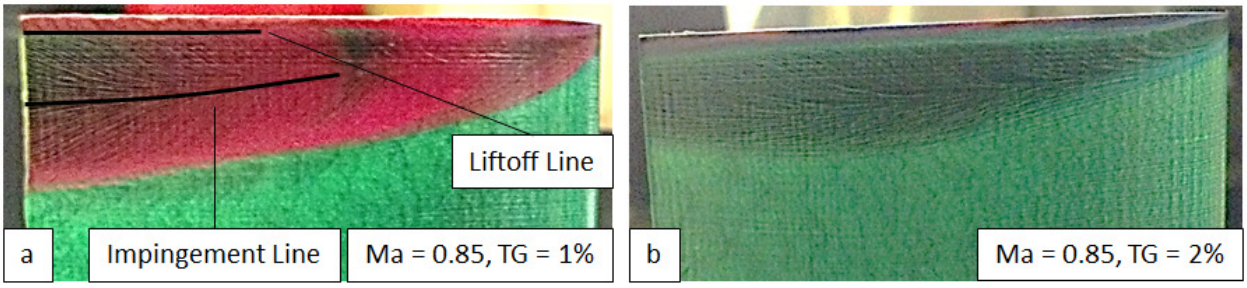

Figure 8. Squealer tip suction side flow visualization results at an exit Mach number of 0.85, a blowing ratio of 1.0 and tip clearance gaps of (a) 1% and (b) 2%

Heat Transfer Results

Flat tip heat transfer coefficient results at an exit Mach number of 0.85 and tip clearance gaps of 1% and 2% are presented in Figure 9, which are similar to those reported by Anto et al [9]. While Macor was used in Anto et al. [9] experiment, ABS was used in the current set of results because of its reduced thermal conductivity which improves the validity of the one-dimensional conduction assumption used in the calculation of heat flux. A linear regression data reduction technique was also used, which is similar to the technique described in this study, as opposed to the method documented by Ekkad et al. [23]. Their method approximates the incoming air temperature profile as a step change and does not adequately represent transient

conditions. Similar trends are observed to those of Anto et al. [9] and are presented for a comparison to squealer tip heat transfer results.

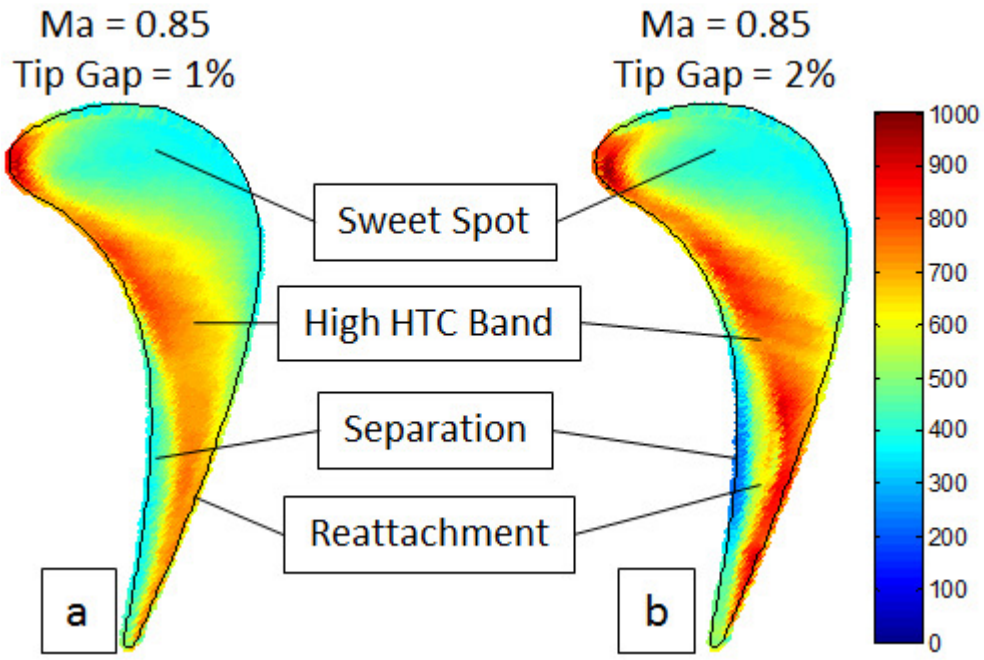

Figure 9. Flat tip heat transfer coefficient results at an exit Mach number of 0.85 and tip clearance gaps of (a) 1% and (b) 2%

For the flat tip blade, as exit Mach number and tip clearance gap increase, the heat transfer coefficient across the tip surface increases. The maximum heat transfer coefficient is observed in the leading edge region where mainstream flow interacts directly with the blade tip without being diverted by the turning flow within the cascade. Corresponding to the "sweet spot" region observed in Figure 4, an area of low heat transfer coefficient exists just downstream of the leading edge. A low pressure gradient between the pressure and suction sides in this region accounts for the low heat transfer coefficients observed. In the mid-chord region, a large band of high heat transfer coefficient is present and is caused by the maximum pressure gradient across the blade tip being located in this region. Towards the trailing edge, mainstream flow reattaches causing a high heat transfer coefficient region to develop. Low heat transfer coefficients are observed along the trailing edge portion of the pressure side due to the presence of flow separation which prevents direct interaction between the mainstream flow and blade tip.

The current flat tip study compares well with the study conducted by Zhang et al .[10], who compared heat transfer and Mach number distributions of a flat tip blade at three tip clearance gaps. Their geometry, as compared to the current study, had an extended trailing edge

region where supersonic flow dominated and a compacted leading edge region where the flow was subsonic. Because of our extended leading edge region, the flow features observed in the current study are compacted in the leading edge and extended in the trailing edge of Zhang et al. [10] blade tip.

Figures 10 and 11 correspond to the heat transfer coefficient and film cooling effectiveness distributions of a squealer tip blade with purge flow blowing at a blowing ratio of 1.0, an exit Mach number of 0.85 and tip clearance gaps of 1% and 2%. In the 1% tip clearance gap case, Figure 10a, the data in the recirculation region to the left of the leading edge purge hole is omitted due to the presence of a negative heat transfer coefficient. This negative heat transfer coefficient is believed to be erroneously calculated due to the close proximity of the tip surface and purge hole to the infrared window causing the infrared camera to measure the temperature of the infrared window and as opposed to the blade tip surface. This observation is supported when compared to the 2% tip clearance gap case, Figure 10b, where the recirculation regions have not been omitted. Near the end of the testing schedule, air and small amounts of water leftover from oil-flow visualization tests began permeating through the surface of the tip in the trailing edge region. As a result the heat transfer coefficients are much lower and not representative of their actual values. For this reason, some trailing edge results are omitted. Edge points in the upstream suction side region have also been omitted due to the data reduction method.

For increasing tip clearance gap from 1% to 2% of the scaled engine blade span at an exit Mach number of 0.85, slightly different heat transfer patterns appear. The major contributor to the difference in heat transfer patterns, in Figure 10, is the increase in leakage flow associated with an increased tip clearance gap. The heat transfer coefficient on the leading edge increases, especially along the pressure side, while the suction side is not significantly changed. Rib and bleeder cavity heat transfer coefficients increase significantly, while cavity heat transfer coefficients decrease. Film cooling effectiveness, in Figure 11, decreases significantly with tip clearance gap, due to an increase in purge flow lost to the increased leakage flow.

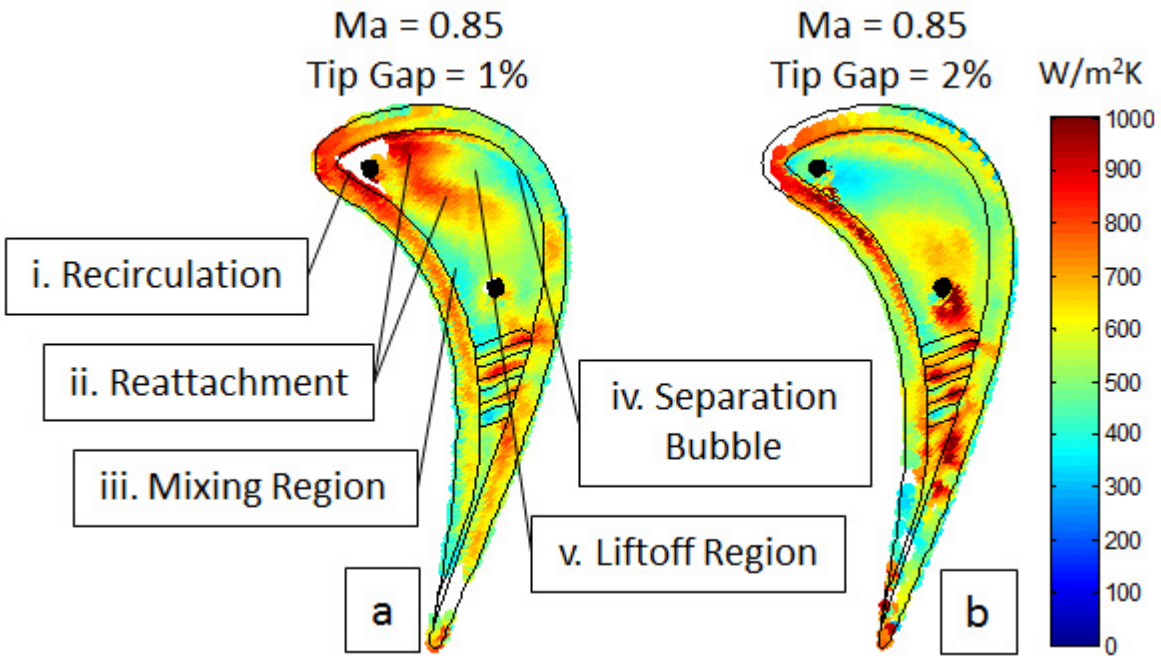

Figure 10. Squealer tip heat transfer coefficient results at an exit Mach number of 0.85, a blowing ratio of 1.0 and tip clearance gaps of (a) 1% and (b) 2%

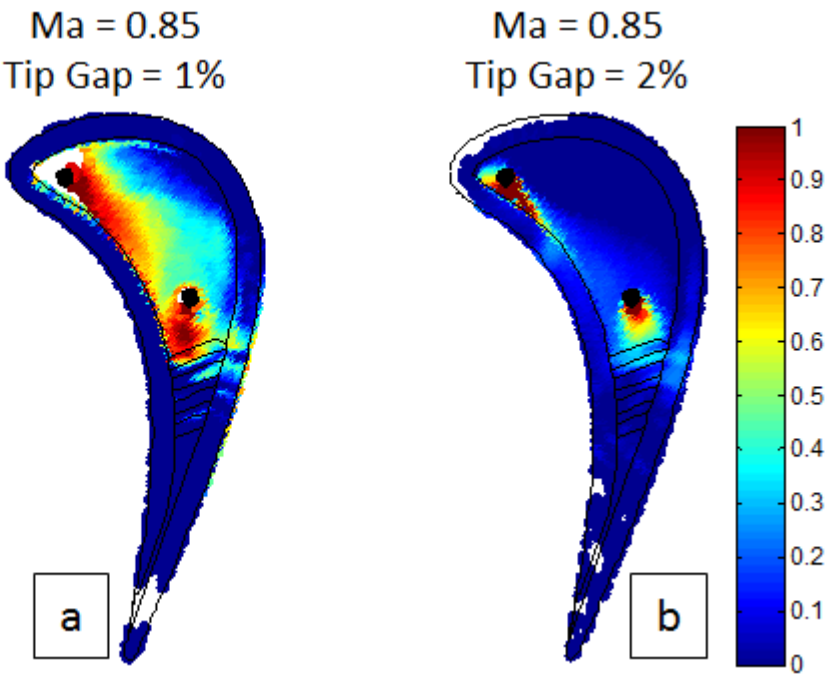

Figure 11. Squealer tip film cooling effectiveness results at an exit Mach number of 0.85, a blowing ratio of 1.0 and tip clearance gaps of (a) 1% and (b) 2%

Corresponding to the two reattachment regions observed in Figure 6a-ii, two high heat transfer coefficient regions are present in Figure 10a-ii. The liftoff region created by the two

reattaching flows corresponds with a low heat transfer coefficient region. Heat transfer coefficient on the suction side rim in this region is low due to the separation bubble created when the reattaching mainstream flow is diverted by the suction side rim. A small region of high heat transfer coefficient is present on the suction side rim just downstream of the separation bubble and corresponds with the location where cavity pigment accumulates in Figure 6. This high heat transfer coefficient region is caused by reattaching mainstream flow that has been channeled downstream by the separation bubble.

Along the suction side rim, a low heat transfer coefficient band is present due to accelerating downstream flow of the air within the cavity. The support ribs help direct flow from the suction to pressure side; however, the presence of a rounded rib end leading to a concave point, on the right side of the first rib, creates a turbulent tripping point that has high heat transfer coefficient and low film cooling effectiveness.

Downstream of the leading edge a recirculation region is observed, where cooling air pools, as evidenced by the approximately zero heat flux values observed. Some of the purge flow cooling air travels downstream along the inside of the pressure side rim, where its effectiveness does not combine with that of the second purge hole. Flow just above of the second purge hole is directed downstream and towards the pressure side, resulting in the low heat transfer coefficient and high film cooling effectiveness region observed just upstream of the pressure side portion of the first support rib. A low heat transfer coefficient, low film cooling effectiveness region corresponding to the mixing region of the pressure and suction side rim flows is observed.

A clockwise, as viewed from the trailing edge, recirculation region develops in the bleeder cavity as a result of the mainstream flow crossing above. Bleeder cavity air is drawn into the mainstream flow along the inside of the pressure side rim and directed upstream. This upstream flow is caused by a negative pressure gradient which forms when the lost bleeder cavity air is replaced by air supplied by the bleeder opening at the trailing edge. The bleeder air helps passively cool the last rib.

For the 2% tip clearance gap case, the two reattachment regions present in the 1% case are significantly diminished in size and magnitude. Increasing tip clearance gap diverts the lower reattachment region and liftoff line downstream. Film cooling effectiveness around the first purge hole is directed towards the pressure side and is characteristic of a recirculation

region. This recirculation region is much smaller than that observed in the 1% tip clearance gap case due to an increase of purge flow blowing air lost to the mainstream flow. While the first purge hole has less of a direct effect on tip heat transfer, its presence along with the downstream trend of an increased tip clearance gap diminishes the effect of the upper reattachment region.

Near the second purge hole a complex flow region is observed due to the close proximity of the reattachment region, purge hole and support ribs. The hot reattaching air is mixed with that of the purge flow to create a high heat transfer coefficient and high film cooling effectiveness region, where turbulent flow is tripped by the proximity of the concave rib cavity. Recirculation around the second purge hole is not as strong as the 1% tip gap cases as evidenced by the suction side direction of the film cooling effectiveness distribution. Film cooling has an effect on the pressure side rim around mid-chord, where cooling air from the first purge hole replaces mainstream flow diverted by the second purge hole. High heat transfer coefficient regions on the pressure side of the second rib and suction side of the third rib are caused by reattachment of mainstream flow along a streamline. Upstream bleeder cavity flow is diminished and causes an increased heat transfer coefficient region on the suction side rim.

When compared to the results presented by Kwak et al. [11], the trends of increasing tip clearance gap correlating to an increase in heat transfer coefficient and a decrease in film cooling effectiveness hold. Ameri et al. [12] observed similar upstream cavity flow circulation down the pressure and suction side rims, however, the presence of the support ribs in the current study inhibit the cavity flow structure from directly affecting the trailing edge results.

Comparison of Flat to Squealer Tip with Purge Flow Blowing

Presented above in Figures 5a and 8a, the leakage vortex impingement line of the flat and squealer tip blade lies approximately 19.5% and 15.4% of the engine blade span from the tip of the blade, respectively, for the 1% tip clearance gap cases. This suggests that there is less leakage flow across the squealer tip blade as compared with the flat tip. The near-tip region of the squealer tip was also significantly coated with cavity pigment suggesting that, without purge flow blowing the leakage vortex would be smaller. With less leakage flow the efficiency of the turbine will increase, however, with the addition of purge flow blowing, this advantage may be lessened because compressed air from the compressor is used to provide the cooling air.

Figure 12 divides the blade into the total cavity including ribs, cavity camber up and camber down and pressure and suction side regions and corresponds to the plots in Figures 13

and 14. Figures 13 and 14 present the average circumferential heat transfer coefficient for the flat and squealer tip cases and the average circumferential film cooling effectiveness results for the squealer tip at an exit Mach number of 0.85 and tip clearance gaps of 1% and 2%, respectively. The local heat transfer coefficients and film cooling effectiveness values are averaged at various x/C_x locations for each of the regions in Figure 12. The dotted lines mark the beginning and end of the rib region.

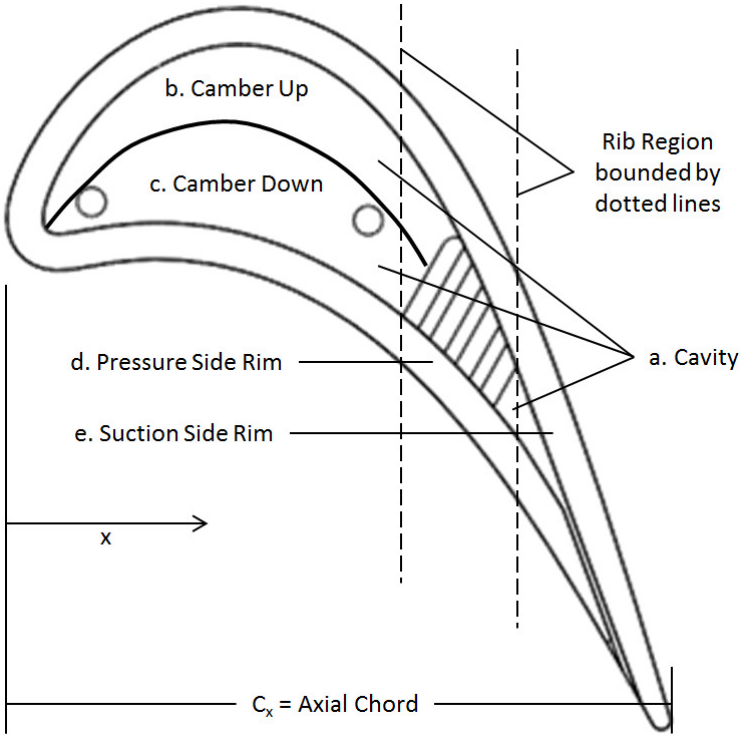

Figure 12. Regions for averaged circumferential results, corresponding to Figures 13 and 14

The cavity camber regions of the 1% tip clearance gap case, Figure 13a, shows that the heat transfer coefficient is higher for the squealer tip case as compared with the flat tip case. However, the regions where there is a significant difference are those in which film cooling effectvieness is quite high, suggesting that thermal failure in these regions is unlikely. Downstream of the camber cavity section, the rib circumferential averaged heat transfer coefficient is less than the corresponding flat tip region and there is also film cooling present suggesting an improvement in heat transfer in this area. In the pressure side rim region, Figure 13d, similar trends to the flat tip heat transfer coefficient are observed, while the effect of purge flow blowing is absent. The maximum pressure side heat transfer coefficient value is observed at the leading edge and is comparable between the flat and squealer tip cases. The squealer tip

case shows higher heat transfer coefficient values along the suction side rim. These high suction side heat transfer coefficient values are not accompanied by the large film cooling effectiveness levels observed within the cavity but are lower than that of the pressure side, therefore , the suction side rim is not an area of concern for thermal failure. The rib region appears to follow the same trend of corresponding high heat transfer coefficient and high film cooling effectiveness.

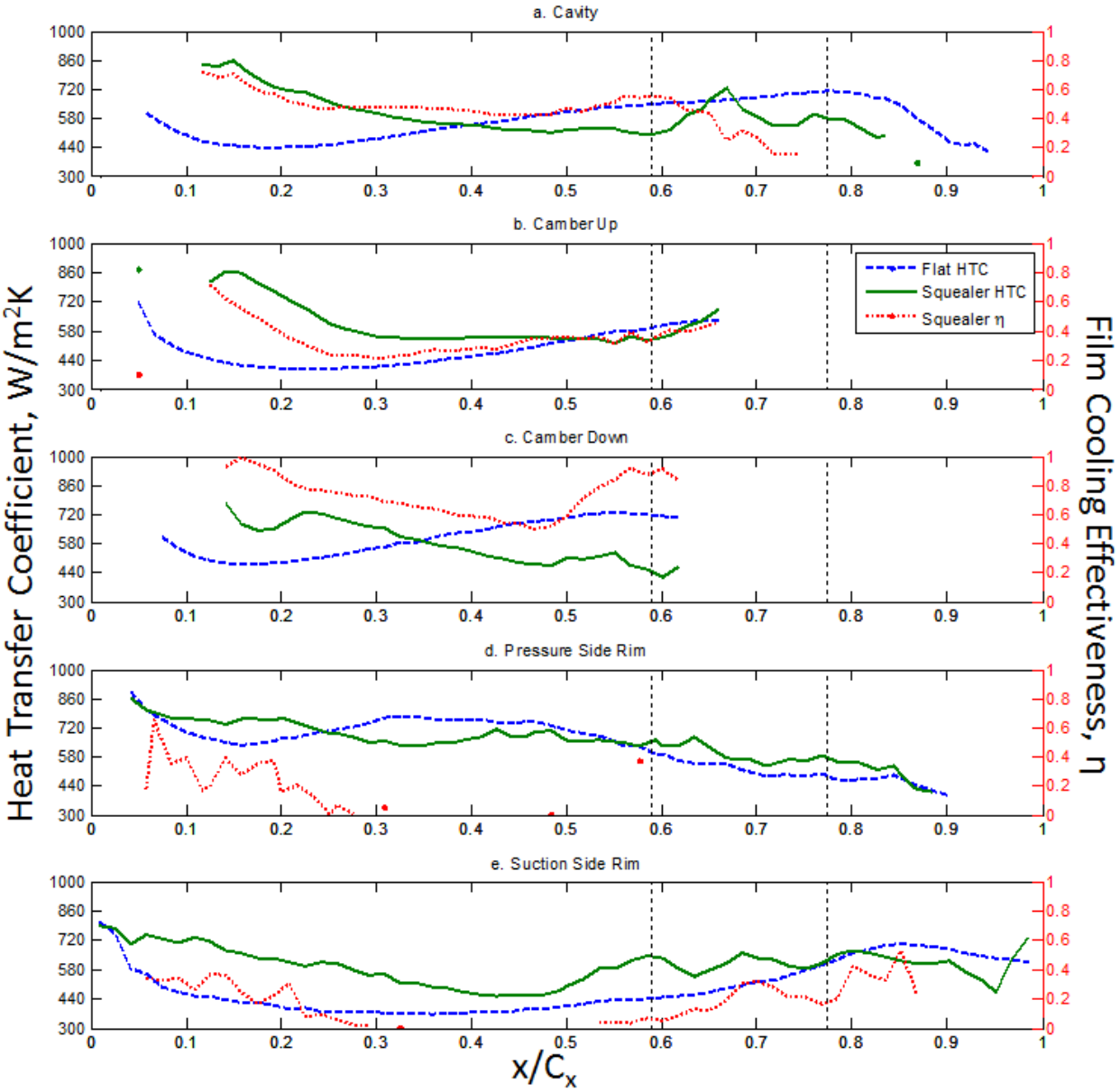

Figure 13. Circumferential averaged heat transfer coefficient and film cooling effectiveness results by region for flat and squealer tip blades at an exit Mach number of 0.85 and a tip clearance gap of 1%

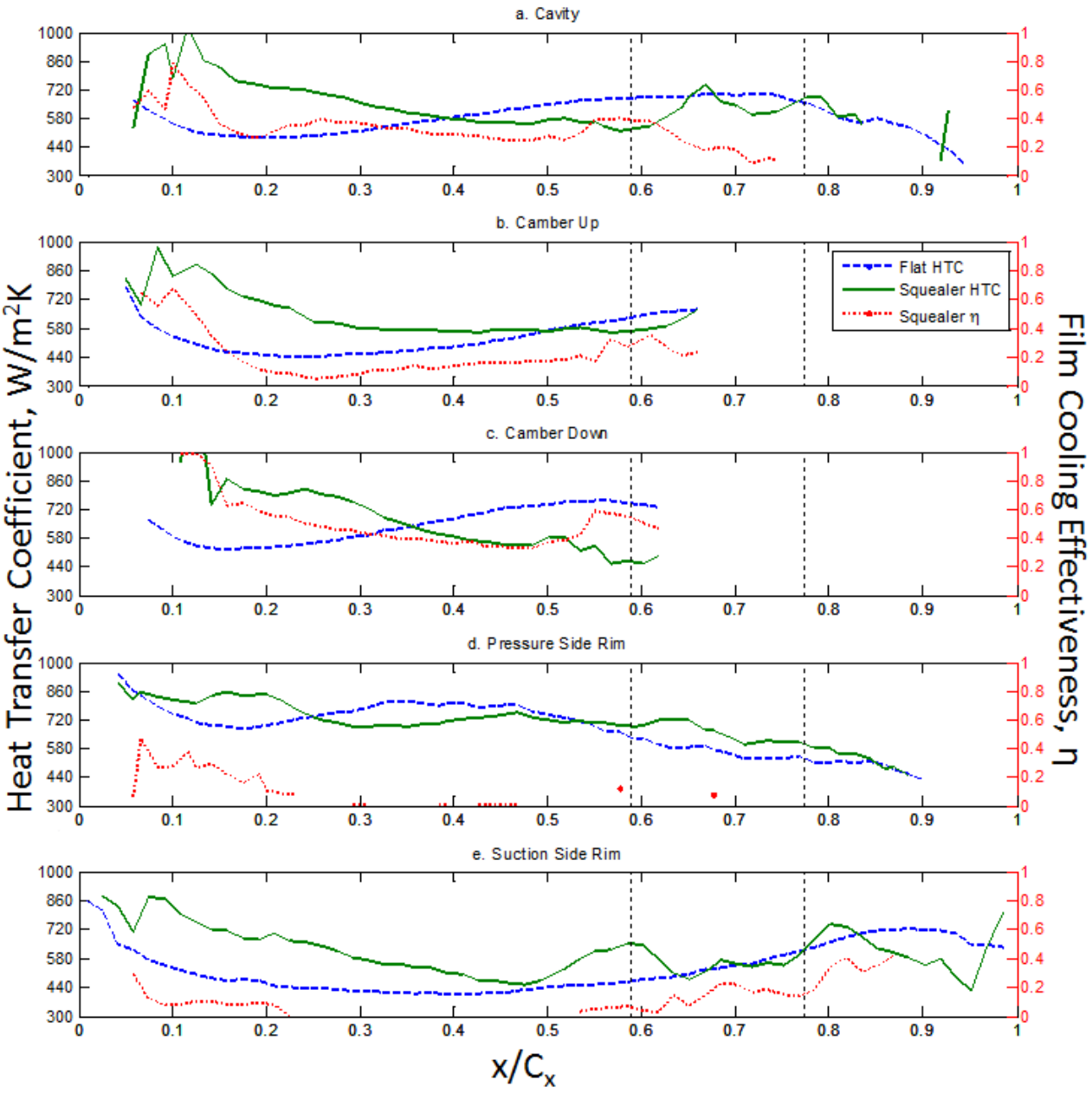

Figure 14. Circumferential averaged heat transfer coefficient and film cooling effectiveness results by region for flat and squealer tip blades at an exit Mach number of 0.85 and a tip clearance gap of 2%

Similar trends are observed for the 2% tip clearance gap case as compared to the 1% case. Figure 14c shows that within the cavity camber regions where the squealer heat transfer coefficient is markedly higher than that of the corresonding flat tip region the film cooling effectiveness is large. However, in the leading edge regions of the pressure and suction side, there are extended areas of high heat transfer coefficient and little to no effect of purge flow

blowing. The rib region observes high heat transfer coefficient levels that are comparable to that of the leading edge, however, the film cooling effectiveness within this region is quite low, suggesting the presense of a high heat transfer area.

Kwak et al. [4] and Azad et al. [5] showed that the addition of a squealer tip resulted in a decrease in the leakage flow, as compared to a flat tip. This reduced leakage flow is observed in the current study as well. The reduced leakage flow had the effect of reducing the heat transfer of the squealer tip blade in the trailing edge region. This result is not observed in the current study due to the presence of the support ribs and the inability of the cavity flow to reach the trailing edge.

Conclusions

The major findings of this experimental study are found below:

1. The maximum heat transfer coefficient location on the flat tip is observed at the leading edge.
2. The maximum heat transfer coefficient locations on the squealer tip are observed at the leading edge, on the support ribs and within the cavity where mainstream flow is reattaching.
3. Cavity heat transfer coefficient values are accompanied by high film cooling effectiveness values and are therefore not likely to see thermal failure.
4. Support ribs have similar heat transfer coefficient values to that of the leading edge and are therefore at risk of thermal failure.
5. Less leakage flow is observed for the squealer tip blade as compared with the flat tip blade.
6. Increasing tip clearance gap results in an increase in average heat transfer coefficient for the flat tip and a decrease for the squealer tip.
7. Increasing tip clearance gap results in a decrease in the average film cooling effectiveness for the squealer tip.

Acknowledgements

This work was conducted with the sponsorship of Dr. H. K. Moon and Dr. L. Zhang of Solar Turbines, Inc. Technical discussions with Dr. Jae Su Kwak of the South Korea Aerospace University and Dr. Song Xue of Techsburg, Inc. were of great help.

References

[1] Bunker, Ronald. "Axial Turbine Blade Tips: Function, Design, and Durability." *Journal of Propulsion and Power* 22.2 (2006): 271-85. Print.

[2] Bunker, R., 2001, "A Review of Turbine Blade Tip Heat Transfer," Ann. N.Y. Acad. Sci., 934, pp. 64-79.

[3] Sjolander, S.A. and Cao, D., 1995, "Measurements of the flow in an idealized turbine tip gap," *ASME J. Turbomach*., 117, pp. 578–584.

[4] Kwak, Jae Su, Jaeyong Ahn, Je-Chin Han, C. Pang Lee, Ronald S. Bunker, Robert Boyle, and Raymond Gaugler. "Heat Transfer Coefficients on the Squealer Tip and Near-Tip Regions of a Gas Turbine Blade with Single or Double Squealer." *Journal of Turbomachinery* 125.4 (2003): 778-87. Print.

[5] Azad, GM S., Han, J. C., Bunker, R. S., and Lee, C. P., 2002, ''Effect of Squealer Geometry Arrangement on a Gas Turbine Blade Tip Heat Transfer,'' ASME J. Heat Transfer, **124**, pp. 452–459.

[6] Mayle, R. E., and Metzger, D. E., 1982, ''Heat Transfer at the Tip of an Unshrouded Turbine Blade,'' *Proc. Seventh Int. Heat Transfer Conf.*, Hemisphere Publishing, Washington, DC, pp. 87–92.

[7] Kline, S.J. and McKlintock, F.A., "Describing Uncertainties in Single sample Experiments," Mechanical Engineering, 75, Jan. 1953, pp. 3-8.

[8] Yang, Dianliang, Xiaobing Yu, and Zhenping Feng. "Investigation of Leakage Flow and Heat Transfer in a Gas Turbine Blade Tip With Emphasis on the Effect of Rotation."*Journal of Turbomachinery* 132.4 (2010): 041010-1-041010-9. Print.

[9] K. Anto, S. Xue and W.F. Ng, L.J. Zhang and H.K. Moon, "Effects of Tip Clearance Gap and Exit Mach Number on Turbine Blade Tip and Near-Tip Heat Transfer," Proceedings of ASME Turbo Expo GT2013-94345.

[10] Zhang, Q., D.O O'Dowd, L. He, M.L.G Oldfield, and P.M. Ligrani. "Transonic Turbine Blade Tip Aerothermal Performance With Different Tip Gaps—Part I: Tip Heat Transfer." *Journal of Turbomachinery* 133.4 (2011): 1041027-1-041027-9. Print.

[11] Kwak, Jae Su, and Je-Chin Han. "Heat Transfer Coefficients and Film Cooling Effectiveness on the Squealer Tip of a Gas Turbine Blade." *Journal of Turbomachinery* 125.4 (2003): 648. Print.

[12] Ameri, A. A., E. Steinthorsson, and D. L. Rigby. "Effect of Squealer Tip on Rotor Heat Transfer and Efficiency." *Journal of Turbomachinery* 120.4 (1998): 753-59. Print.

[13] Holmberg, D.G., and Diller, T.E., 2005, "Simultaneous Heat Flux and Velocity Measurements in a Transonic Turbine Cascade," ASME J. Turbomach., 127, pp. 502-506. 29.

[14] Nix, A.C., Diller, T.E., and Ng, W.F., 2007, "Experimental Measurements and Modeling of the Effects of Large-Scale Freestream Turbulence on Heat Transfer," ASME J. Turbomach., 129, pp. 542-550.

[15] Smith, D.E., Bubb, J.V., Popp, O., Grabowski, H.C., Diller, T.E. Schetz, J.A. and Ng. W.F., 2000, "Investigation of Heat Transfer in a Film Cooled Transonic Turbine Cascade, Part I: Steady Heat Transfer," ASME 2000-GT-202.

[16] Popp, O., Smith, D.E., Bubb, J.V., Grabowski, H.C., Diller, T.E. Schetz, J.A. and Ng. W.F., 2000, "Investigation of Heat Transfer in a Film Cooled Transonic Turbine Cascade, Part II: Unsteady Heat Transfer," ASME 2000-GT-203.

[17] Carullo, J. S., Nasir, S., Cress, R. D., Ng, W. F., Thole, K. A., Zhang, L. J., and Moon, H. K., 2011, "The Effects of Freestream Turbulence, Turbulence Length Scale, and Exit Reynolds Number on Turbine Blade Heat Transfer in a Transonic Cascade," ASME J. Turbomach., 133, 011030.

[18] Nasir, S., Carullo, J.S., Ng, W.F., Thole, K.A., Wu, H., Zhang, L.J., and Moon, H.K., 2009, "Effects of Large Scale High Freestream Turbulence, and Exit Reynolds Number on Turbine Vane Heat Transfer in a Transonic Cascade," ASME J. Turbomach., 131, 021021.

[19] Cress, R. D., 2006, "Turbine Blade Heat Transfer Measurements in a Transonic Flow Using Thin film Gages," *Master's Thesis, Virginia Polytechnic Institute and State University.*

[20] Xue, Song. *Fan-Shaped Hole Film Cooling on Turbine Blade and Vane in a Transonic Cascade with High Freestream Turbulence: Experimental and CFD Studies*. Diss. Virginia Polytechnic Institute and State University, 2012. N.p.: n.p., n.d. Print.

[21] Cook, W. J., and E. M. Felderman. "Reduction of Data from Thin-film Heat-transfer Gages - A Concise Numerical Technique." *AIAA Journal* 4.3 (1966): 561-62. Print.

[22] Moffat, R. J., 1988, "Describing Uncertainties in Experimental Results," *Exp. Thermal and Fluid Science*, 1988, pp. 3-17.

[23] Ekkad, S. V., Ou, S., and Rivir, R. B., 2004, "A Transient Infrared Thermography Method for Simultaneous Film Cooling Effectiveness and Heat Transfer Coefficient Measurements From a Single Test," *ASME J. Turbomach*., 126, pp. 546–553.

Appendix A: Cascade Setup

ABS Tip of the Center Test Blade

Figure 15 shows the ABS squealer tip used on the center three blades in the cascade. The tips have a span of 1.5 inches (38.1 mm) and were printed using the Fortus 250mc rapid prototyping machine by Stratasys. Screwed into the base of the tip are cooling air supply and pressure tap tubes leading to the plenum inside the tip. These tubes were fabricated by drilling a hole through steel plugs and silver soldering an airtight seal around the base of the plug.

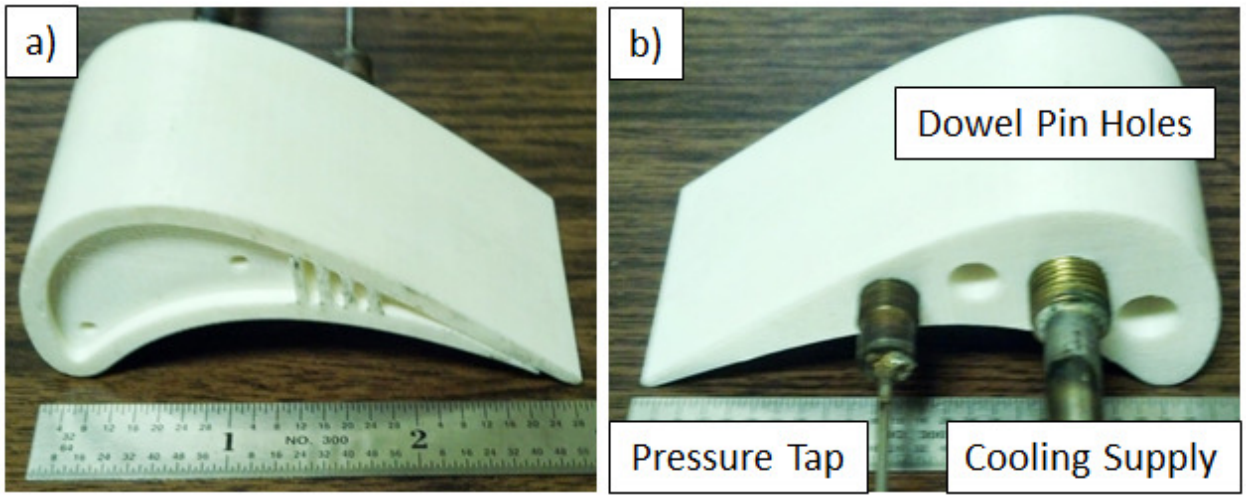

Figure 15. ABS tip of the test blade

Stainless Steel Base of the Center Test Blade

Figure 16 shows the stainless steel base used on the center three blades in the cascade. The bases have holes for passing the cooling air supply and pressure tap tubes through their span of 4.5 inches (114.3 mm), along with tapped mounting and dowel pin holes.

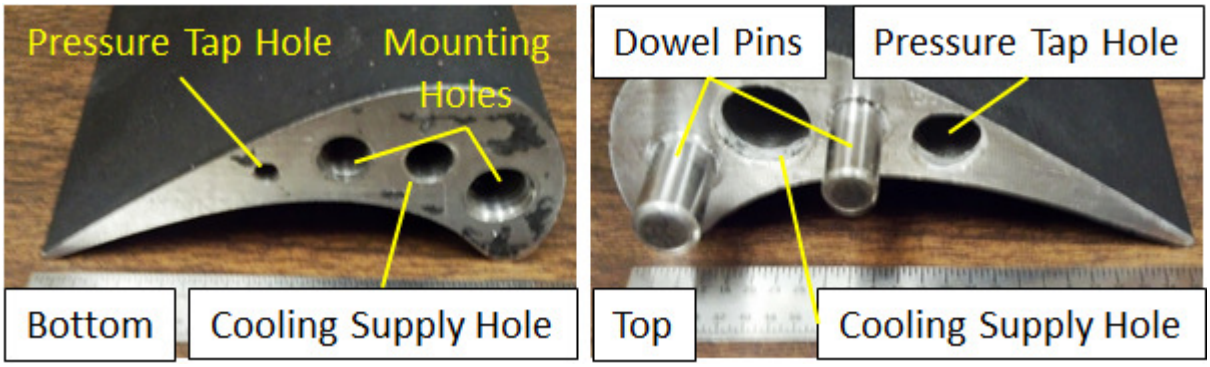

Figure 16. Stainless steel base of the test blade

Fully Assembled Center Test Blade

Figure 17 shows the completed blade where the ABS tip and stainless steel base are attached with dowel pins and JB Weld. The cooling supply and pressure tap tubes pass from the ABS tip through the stainless steel base. The ABS tip was sealed to avoid leaks from the by brushing Acetone and then Ambroid Pro-Weld, a plastic epoxy, onto the surface of the blade. Upon sealing, the blades were painted with flat black spray paint and sanded with a fine grit sandpaper to ensure accurate measurement by the IR camera.

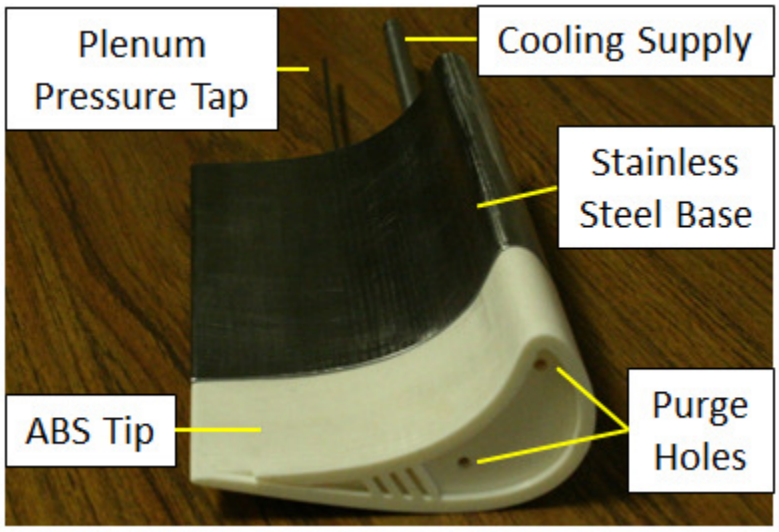

Figure 17. Squealer tip blade with purge flow cooling supply and plenum pressure tap

Mounting and Adjustment of Blade Tip Clearance in the Test Section

Figure 18 shows a CAD drawing the test section window where the blades have been mounted. The cascade consists of seven blades, where the top and bottom two blades are supported from both sides by two circular windows. To ensure the center and adjacent blades have the same tip gap; the three blades are attached to same insert block. All three squealer tip blades are cantilevered and have their respective cooling air supply and pressure tap tubes passing through the insert block. The four corner bolts on the insert block, colored in red, are used to achieve different tip gaps. When the appropriate tip gap has been set the ten other bolts, colored in blue, are used to hold the insert block in position for the duration of the tunnel run. Figure 19 shows the completed center and adjacent blades in the test section during installation.

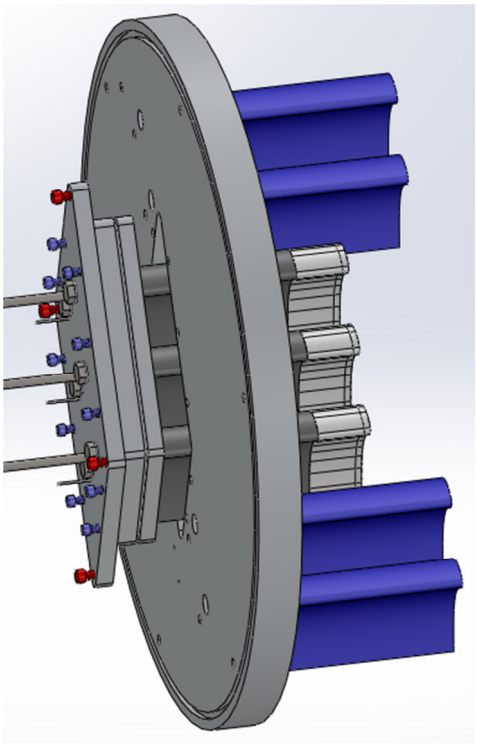

Figure 18. Tip gap adjustment hardware

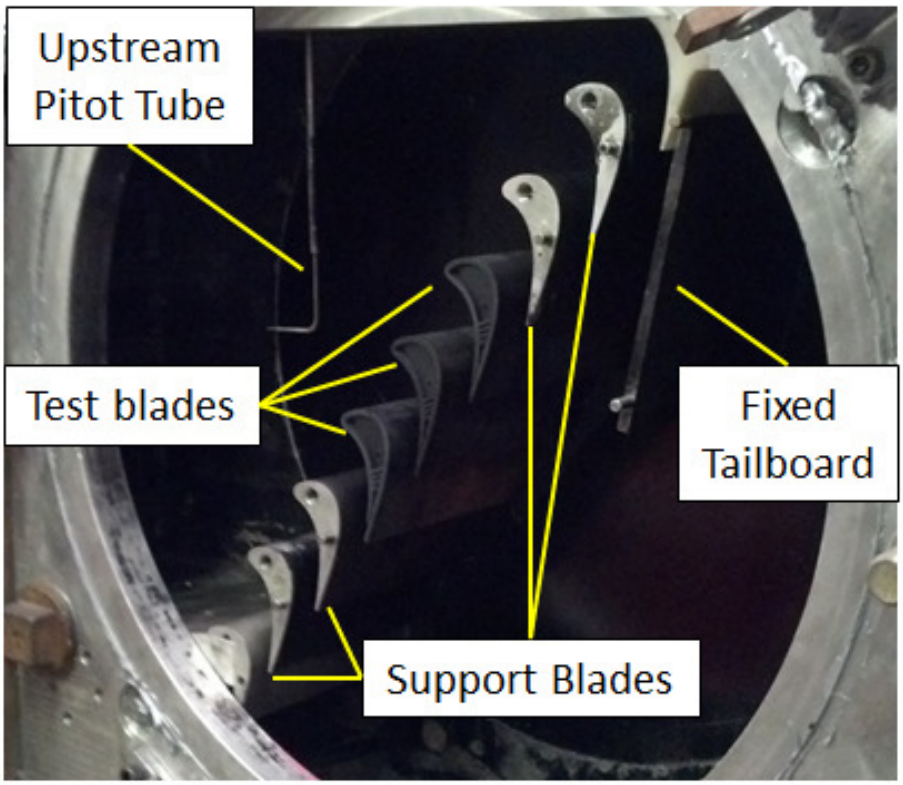

Figure 19. Test section with squealer tip blades installed

Appendix B: Tunnel Condition Calculation

Downstream Static Pressure Tap Layout

Six static pressure ports were drilled into the circular test section window 0.5 C downstream, as shown in Figure 20. The static pressure port numbers are used in conjunction with Figure 21. The downstream static pressure ports along with the upstream total and static pressures, measured by a Pitot tube located 2.2 C in front of the leading edge, are used to calculate the inlet and exit Mach numbers. The downstream static pressure ports are also used to determine flow periodicity.

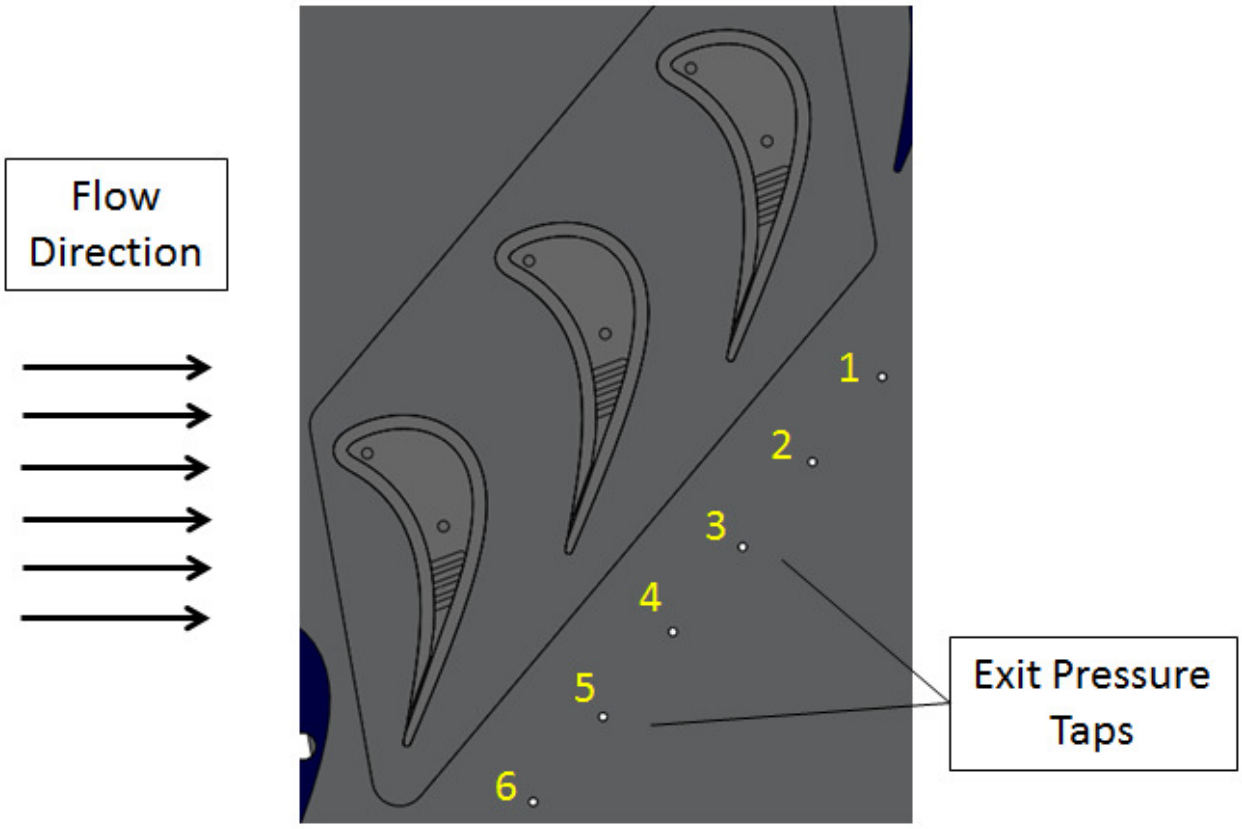

Figure 20. Endwall pressure tap locations in relation to blade geometry

Static Pressure Measurement Technique

A Model 98RK Net Scanner System is used throughout the experiment to record pressure measurements at 10 Hz. The flow through the tunnel is assumed isentropic; therefore the upstream and downstream total pressures are the same. Downstream static pressure measurements from the six pressure taps are averaged at each time step. This new average static

pressure is used with the downstream total pressure to calculate the exit Mach number at each time step using Equation B.1, where γ is the specific heat ratio of air, P_o is the stagnation or total pressure of the fluid and P_s is the static pressure.

$$Ma = \sqrt{\frac{2}{\gamma - 1}\left(\left(\frac{P_o}{P_s}\right)^{\frac{\gamma-1}{\gamma}} - 1\right)} \tag{B.1}$$

The upstream Mach number can also be calculated using equation B.1 and using the upstream static pressure as measured by the Pitot tube. The Mach number is calculated at each time step and after the initial ramp up time is averaged for 2 seconds. This averaged Mach number is reported as the exit Mach number.

Blowing Ratio Measurement Technique

The experiments were conducted using one blowing ratio, 1.0. This blowing ratio is calculated using equation B.2, where ρ is the density of the fluid and U is the velocity.

$$BR = \frac{(\rho U)_{coolant}}{(\rho U)_{mainstream,avg}} \tag{B.2}$$

The density and velocity of the coolant are found by calculating the mass flow rate of the coolant, using an orifice meter, and dividing by the purge hole area. The orifice meter mass flow rate equation used is shown in Equation B.3, where C is the meter coefficient equal to 0.8496, $A_{orifice}$ is the orifice area, P_H and P_L are the high and low pressures of the meter, M is the molecular mass of air and R is the universal gas constant.

$$\dot{m}_c = C A_{orifice} P_H \sqrt{\frac{2\,M}{Z\,R\,T_c}\left(\frac{\gamma}{\gamma - 1}\right)\left[\left(\frac{P_L}{P_H}\right)^{2/\gamma} - \left(\frac{P_L}{P_H}\right)^{\gamma+1/\gamma}\right]} = (\rho U A)_c \tag{B.3}$$

The orifice meter is located upstream of where the coolant flow is split into the three streams for each of the squealer tip blades. This total mass flow rate is divided by three to find the coolant mass flow rate for each of the blades. The pressure and temperature of the cooling air is measured in the plenum just before entering into the test section and the recorded values have less than a 3% difference.

The density and velocity of the mainstream flow is averaged for the inlet and exit of the blades and calculating the properties of the flow is done using the same technique. Equation B.1

is used to find the Mach number and this is used in conjunction with the total temperature upstream, same as the total temperature downstream due to isentropic assumption, to find the static temperatures, as shown in Equation B.4.

$$T_s = \frac{T_o}{1 + \frac{\gamma - 1}{2} Ma^2} \tag{B.4}$$

The speed of sound, velocity and density of the mainstream flow is then calculated using Equations B.5, B.6 and B.7, respectively. The density and velocity at the inlet and exit of the blades is averaged at each time step and used in Equation B.1. A two second time window is used after the initial ramp up time in the tunnel and the blowing ratio reported is the average for those two seconds.

$$Speed\ of\ Sound = SoS = \sqrt{\gamma \frac{R}{M} T_s} \tag{B.5}$$

$$U = Ma * SoS \tag{B.6}$$

$$\rho = \frac{P_s\, M}{T_s\, R} \tag{B.7}$$

Blade Passage Periodicity

Midstream blade passage periodicity has been investigated thoroughly by Nasir et al. [H.1] for the current blade geometry and test setup, therefore an intensive investigation in this experiment is not necessary. However, periodic flow is important and has been monitored throughout the experiment. Figure 21 shows the average exit Mach numbers as measured by the downstream static ports for all tunnel runs. The flow is relatively steady across the passage and therefore periodic for both Mach numbers. However, the flow is less periodic for Mach 1.05 as compared to Mach 0.85. Also, at port 6 the 1% tip gap values are lower than the 2% suggesting that the flow at the bottom of the passage changes more with tip gap than the other portions of the passage.

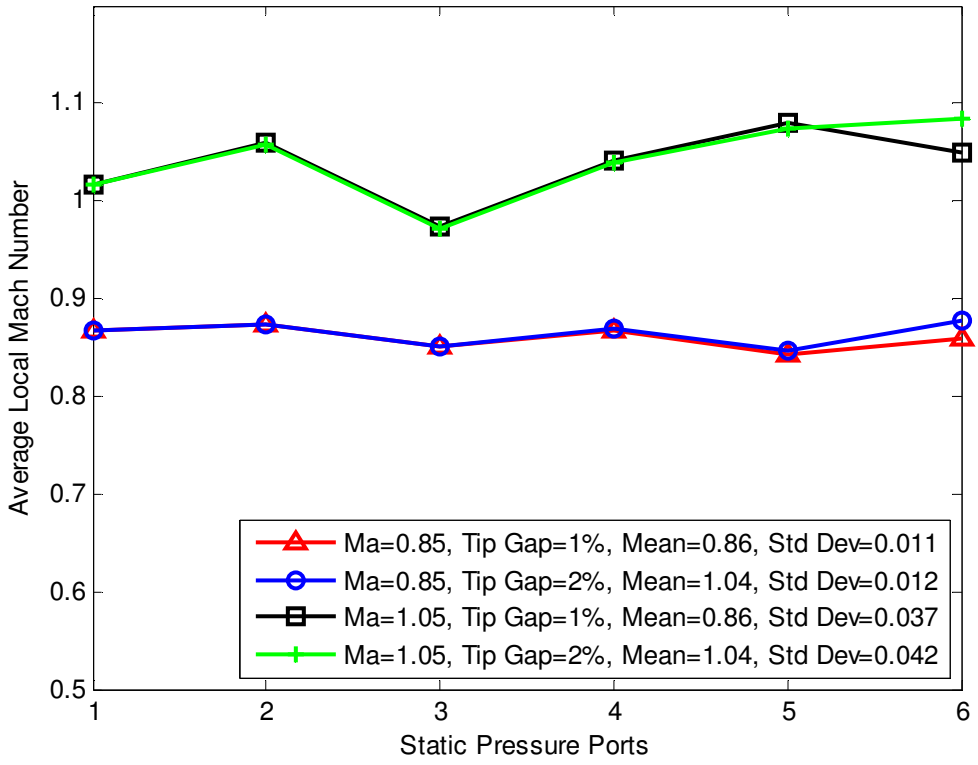

Figure 21. Average local exit Mach number for six downstream static pressure ports and all tunnel runs

Typical Temperature Distributions

For the data reduction method to work, two tunnel runs with two coolant temperatures are needed, Figure 22 shows the typical temperature distribution for a point on the blade tip surface over two tunnel runs. The mainstream total, local recovery, local wall and coolant temperatures are plotted for the duration of a tunnel run. It is observed that the recovery temperature is much lower than the mainstream total temperature. This temperature difference, total inlet minus recovery, can be used to calculate the local Mach number as shown in Equation B.8. The Mach numbers observed are much higher than what is expected and it is therefore believed that the recovery temperatures calculated are too low. The under-prediction of the recovery temperature is caused by a combination of wall temperature measurement errors and the assumption of the mainstream total temperature, average for the tunnel and not local, as the driving temperature within the recovery temperature calculation. Using a boundary layer correction to obtain a more accurate total temperature resulted in a decrease in local Mach

number to reasonable values but increased the heat transfer coefficient dramatically, to levels not observed anywhere in literature. Results with heat transfer coefficients comparable to literature are presented in this study and further investigation into the recovery temperature calculation method is suggested. While the scale of the heat transfer coefficient results is in question the trends observed between different test cases are independent of the temperature difference and total temperatures used, therefore the comparisons reported in this study are unaffected. Film cooling effectiveness is relatively unaffected by changes in the temperature difference and total temperatures used.

$$Ma^2 = \frac{2\,C_p\left(T_{o,\infty} - T_r\right)}{(1 - r_c)\sqrt{\gamma R T_{o,\infty}}} \tag{B.8}$$

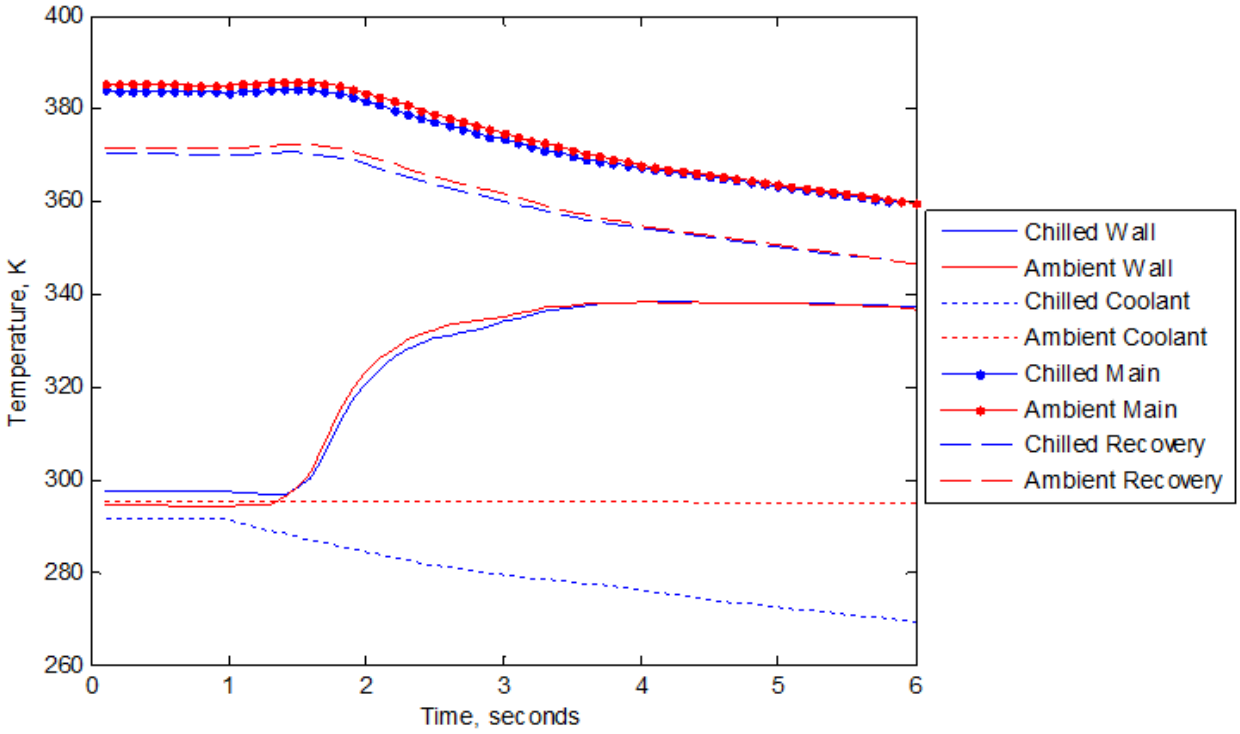

Figure 22. Typical temperature distribution at a single point on the blade surface for two tunnel runs at two different temperature coolants

Appendix C: Infrared Technique

An accurate measure of the surface temperature of the squealer tip blade throughout the duration of a tunnel run is necessary to calculate the heat transfer coefficient and film cooling effectiveness. A FLIR A325 infrared camera is used to capture these images at a sampling rate of 10 Hz. The IR camera uses the blackbody emission radiated from a surface to output that surface's temperature. The test section along with the blade surface was painted black to reduce reflections and increase emissivity. Six months prior to testing the IR camera was calibrated by the manufacturer and upon the manufacturers recommendation the camera was not recalibrated before the experiment. To seal the test section a Zinc Selenide, ZnSe, infrared window was installed in the test section, as shown in Figure 23. The window has had anti-reflective coating applied and transmits about 100% of a 9.3 μm wavelength.

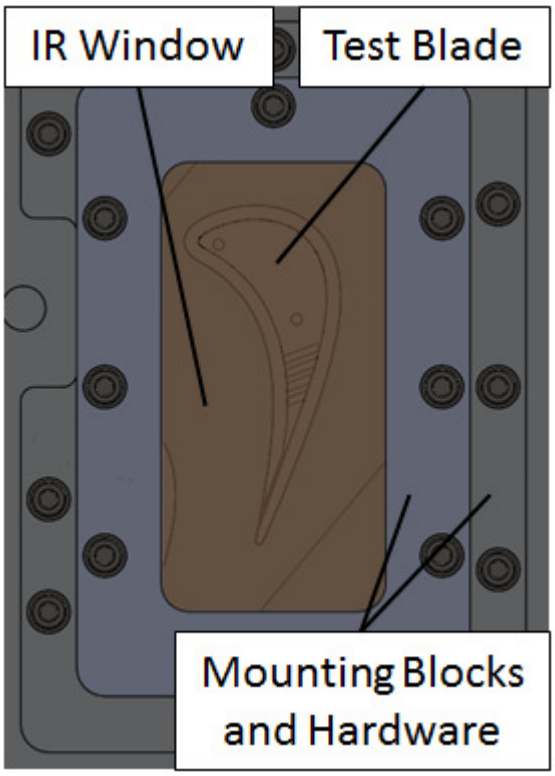

Figure 23. CAD drawing of IR window installed in the test section

Linear Regression Data Reduction

To calculate the heat transfer coefficient, h, and film cooling effectiveness, η, a linear regression technique is employed, where x and y data are known and a linear fit is used to find the slope and y-intercept. Equations C.1 and C.2 are combined to form Equation C.3 by

substituting T_f, the local film temperature. Equation C.3 is used in the linear regression technique, where q''_w is the heat flux, T_c is the coolant temperature and T_w is the surface temperature of the blade. Also, because the Mach numbers being investigated are transonic, T_m is replaced by T_r, the recovery temperature. Finding the recovery temperature will be discussed later.

$$q''_w = h(T_f - T_w) \tag{C.1}$$

$$\eta = \frac{T_f - T_m}{T_c - T_m} \rightarrow T_f = \eta T_c + (1-\eta)T_m \tag{C.2}$$

$$\frac{q''_w}{T_r - T_c} = h\frac{T_r - T_w}{T_r - T_c} - h\eta \rightarrow y = mx + b \tag{C.3}$$

The surface and coolant temperatures are measured directly in the experiment by the IR camera and a thermocouple located in the plenum of the blade, respectively. The heat flux on the surface of the blade is calculated using an implicit, transient finite-difference method, where the energy equation, initial and boundary conditions as given in Equations C.4, C.5 and C.6, respectively. Semi-infinite and one-dimensional conduction assumptions are made in developing this model. The finite-difference code used was developed by Cress [H.2].

$$\frac{\partial T}{\partial t} = \alpha \frac{\partial^2 T}{\partial x^2} \tag{C.4}$$

$$T = T_i \; at \; t = 0 \tag{C.5}$$

$$q''_w(t) = -k\frac{dT}{dx} \; at \; x = 0 \; and \; T = T_i \; as \; x \rightarrow \infty \tag{C.6}$$

The Cook and Felderman [H.3] equation, Equation 9 from the Data Reduction Technique section and Equation C.7 here, can also be used to calculate the heat flux into the blade tip. The finite-difference code is used because the increase in time associated with its use is not significant and its accuracy is within 0.5% of Equation C.7.

$$q''(t_n) = \frac{2\sqrt{k\rho C_p}}{\sqrt{\pi\,\Delta t}} \sum_{j=1}^{n} \frac{T_j - T_{j-1}}{\sqrt{n-j} + \sqrt{n+1-j}} \tag{C.7}$$

Recovery Temperature Calculation

Having calculated the heat flux along the blade tip, the recovery temperature must now be found. To calculate the recovery temperature, at least two tunnel runs have to be matched up. Also, two methods exist which give similar results. The first method uses a tunnel run where there is no purge hole cooling in conjunction with a run where cooling is present. The second method uses two tunnel runs where cooling is present.

A linear regression technique is used in the first method to calculate the recovery temperature at discrete points on the surface of the blade for a no cooling tunnel run. Equation C.8 shows the linear regression equation, where the heat flux is calculated using the same finite-difference method described earlier, and $T_{o,\infty}$ is the total temperature of the mainstream flow as measured in the tunnel run.

$$q''_w = h\left(T_{o,\infty} - T_w\right) - h\left(T_{o,\infty} - T_r\right) \tag{C.8}$$

The recovery temperature is extracted from the ($T_{o,\infty}$ - T_r) term using the total temperature from the cooling run. This recovery temperature is aligned with the same surface points as in the cooling tunnel run, thus supplying the last of the unknown variables to Equation C.3. A third cooling tunnel run at a different cooling temperature can also be used to supply more data points and provide a better fit to the linear regression equation. Figure 24 shows the linear regression fit to the data using the first method.

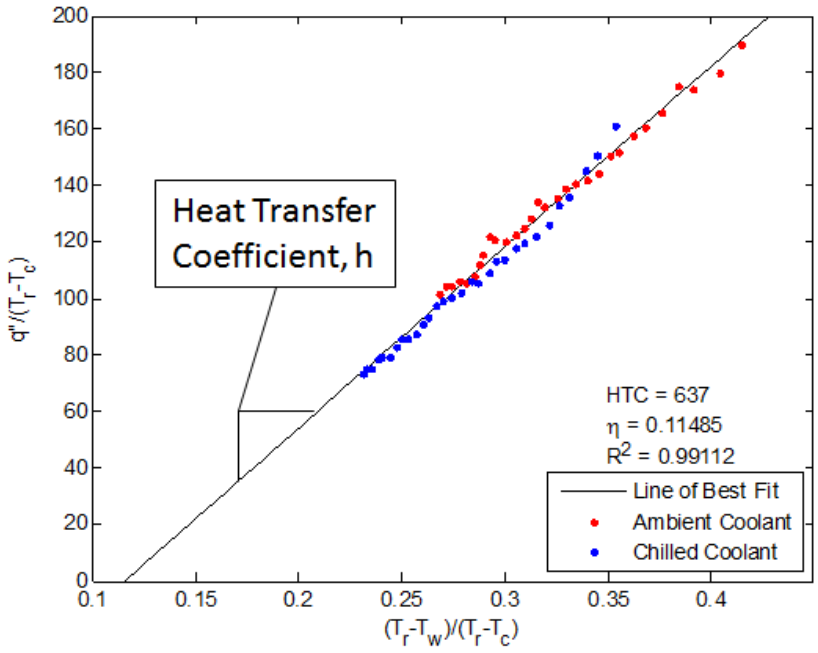

Figure 24. Linear regression fit for the first method of calculating recovery temperature

The second method of finding the recovery temperature uses two tunnel runs with different coolant temperatures. Equation C.9 shows the recovery temperature as a function of total temperature, $T_{o,\infty}$, the local recovery factor, r_c, and local Mach number.

$$T_r = T_{o,\infty}\left(\frac{1 + r_c\frac{\gamma-1}{2}Ma^2}{1+\frac{\gamma-1}{2}Ma^2}\right) = T_{o,\infty}C_r \qquad \text{(C.8)}$$

Exact knowledge of the flow on the squealer tip is not known, so the local recovery factor and Mach numbers cannot be calculated, however the flow condition are considered constant between the two tunnel runs. Therefore, an iterative method of calculating C_r, a parameter representing the term in parenthesis in Equation C.9, is used in conjunction with two cooling runs to linearize the data, based on the linear regression equation and get the coefficient of determination, R^2, as close to one as possible. The coefficient of determination in a linear regression scheme is an indication of how linear the data set actually is and the closer to one R^2 is the better the fit. Figure 25 shows the start and finish of the second linear regression scheme from a solution that is not well fit to one that is.

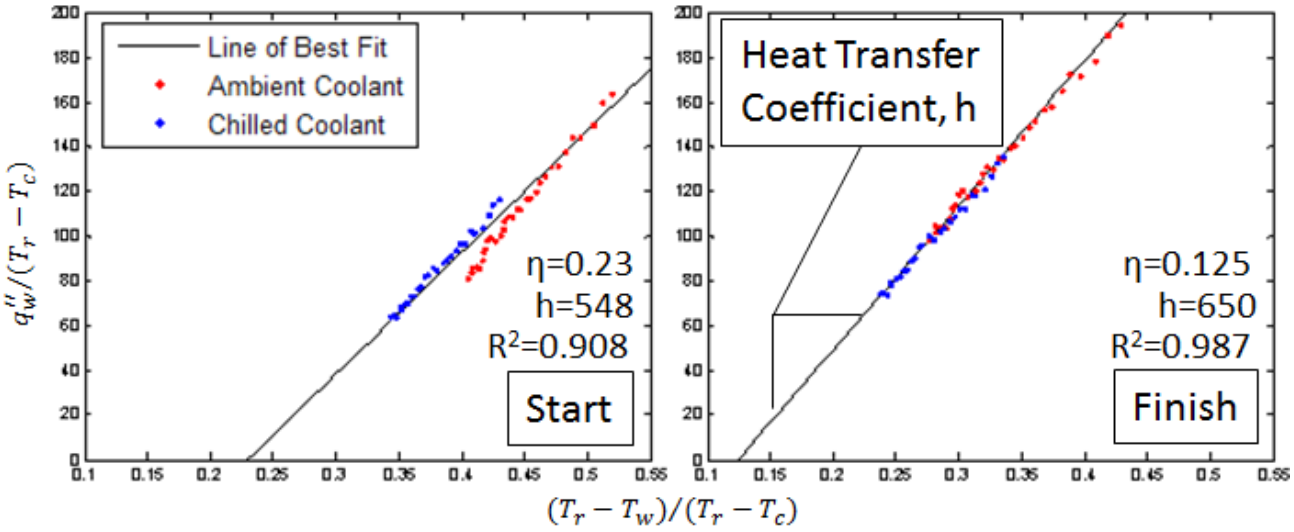

Figure 25. Linear regression progression for the second method of calculating recovery temperature

The process used to produce Figures 24 and 25 is repeated for every data point on the surface of the tip and the two plots were produced using the same data point. The heat transfer coefficient and film cooling effectiveness for the first method are 637 W/m^{2}K and 0.115, while they are 650 W/m^{2}K and 0.125 for the second method. The percent difference in the heat transfer coefficient and film cooling effectiveness of the two methods is approximately 3% and 9%, respectively. Therefore, either method could be used to calculate the heat transfer coefficient and film cooling effectiveness across the entire blade surface. The second method only uses purge flow blowing cases; therefore it is the most representative of the actual flow physics within the tunnel and is the method used in this study.

Near Purge Hole Effect on Wall Temperature

Within the heat transfer coefficient and film cooling effectiveness results, data to the left of the leading edge purge hole has been omitted, for the 1% tip clearance gap cases, where a recirculating coolant region is observed. The results were found to be erroneous due the negative heat transfer coefficient values observed. The negative heat transfer coefficient values are a result of a negative heat flux, calculated within the chilled coolant run. This could be caused by possibly two reasons, first, the data reduction method cannot adequately model a recirculating coolant region, or second, the close proximity of the infrared window to the tip surface and purge hole causes the infrared camera to measure the temperature of the infrared window and not the

blade tip surface. The region of bad data is not observed in the 2% tip clearance gap cases and is significantly lessened in the results at a Mach number of 1.05. Figure 26 shows the wall temperatures at two points on the blade tip, near the leading edge purge hole and away from the purge hole, for chilled runs at a Mach number of 0.85 and tip clearance gaps of 1% and 2%. In the 1% tip clearance gap case, Figure 26a, a lag in the measured wall temperature is present that is not observed away from the purge hole or anywhere in the 2% tip clearance gap results, Figure 26b. Because recirculating coolant is observed in all cases and negative heat transfer coefficient is observed in only the 1% tip clearance gap cases, it is most likely that erroneous heat transfer coefficient is caused by the infrared camera measuring the temperature of the infrared window as opposed to the blade tip surface.

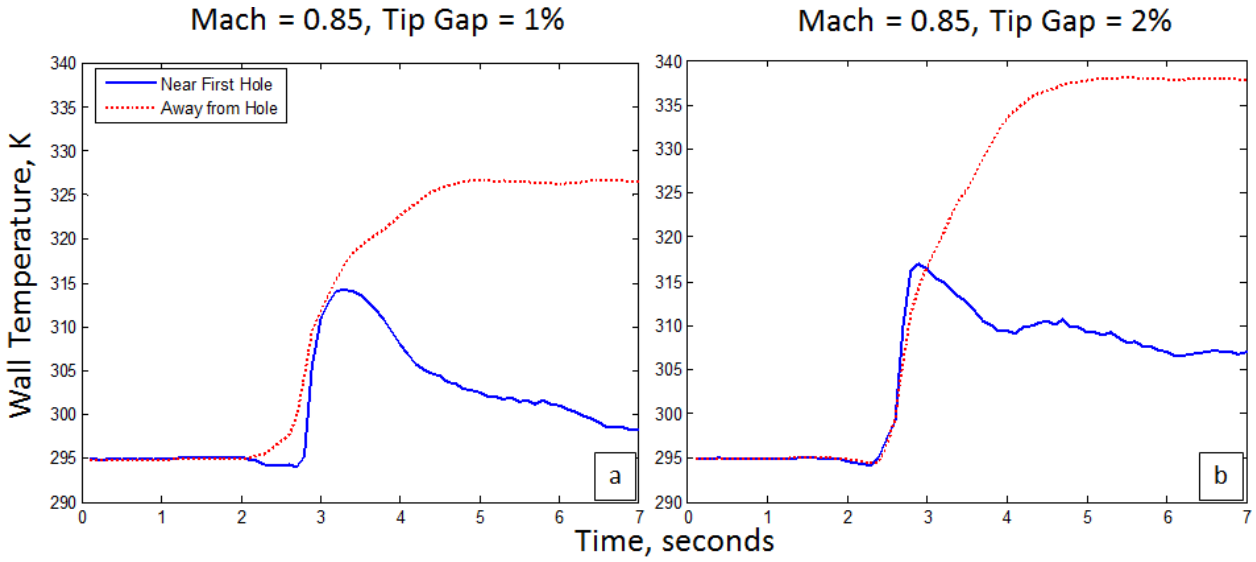

Figure 26. Wall temperature plots for an entire tunnel run at near purge hole and away from purge hole points at tip clearance gaps of 1% and a Mach number of 0.85

Appendix D: Additional Results

Oil Flow Visualization Results

Figures 27 and 28 present the flat tip oil flow visualization results at an exit Mach number of 0.85, originally reported in Anto et al. [H.4]. Figure 27 and 28 correspond to tip and suction side oil flow visualizations, respectively.

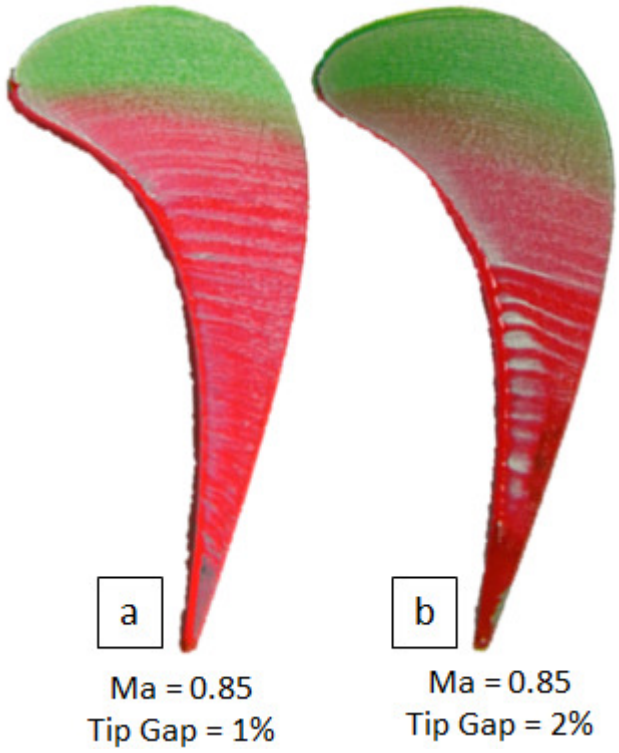

Figure 27. Flat tip oil flow visualization for an exit Mach number of 0.85 and tip clearance gaps of (a) 1% and (b) 2%, as reported by Anto et al. [H-4]

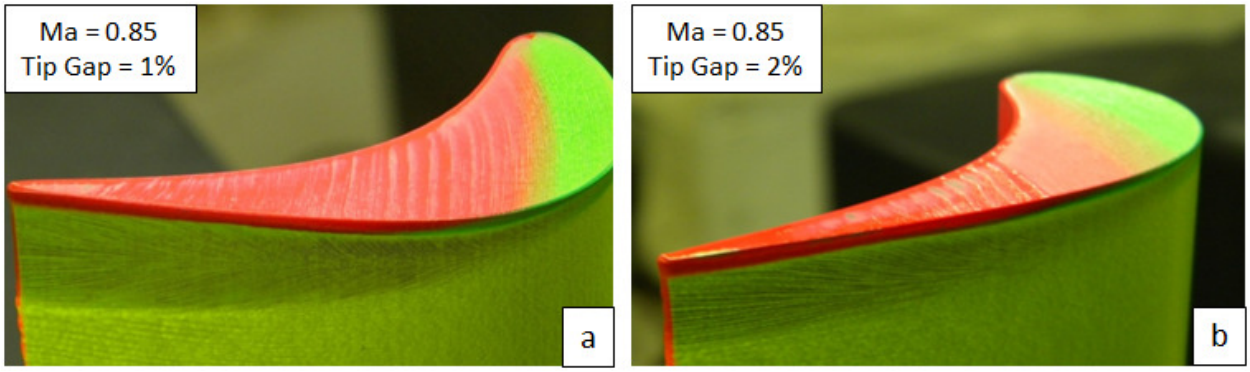

Figure 28. Flat tip suction side oil flow visualization for an exit Mach number of 0.85 and tip clearance gaps of (a) 1% and (b) 2%, as reported by Anto et al. [H-4]

Figures 29, 30 and 31 present the squealer tip oil flow visualizations on the tip, suction side and endwall, respectively, at a blowing ratio of 1.0.

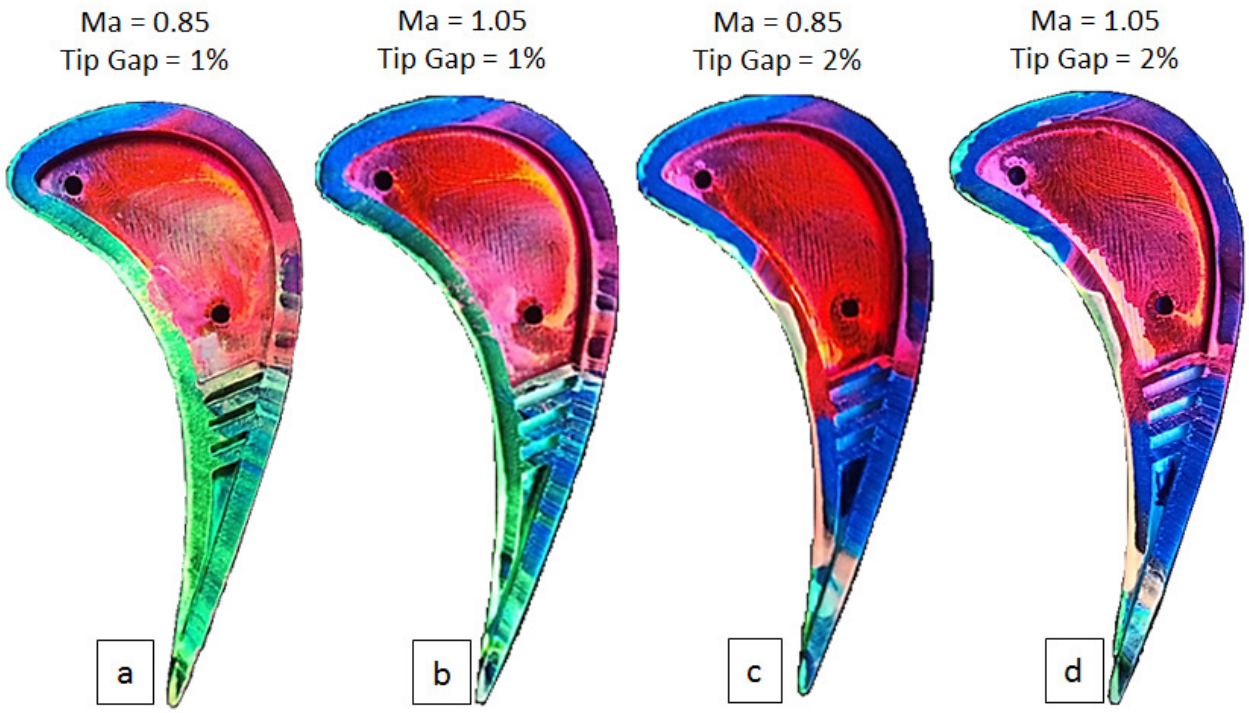

Figure 29. Squealer tip oil flow visualization for Mach numbers of 0.85 and 1.05 and tip clearance gaps of 1% and 2%, at a BR=1.0

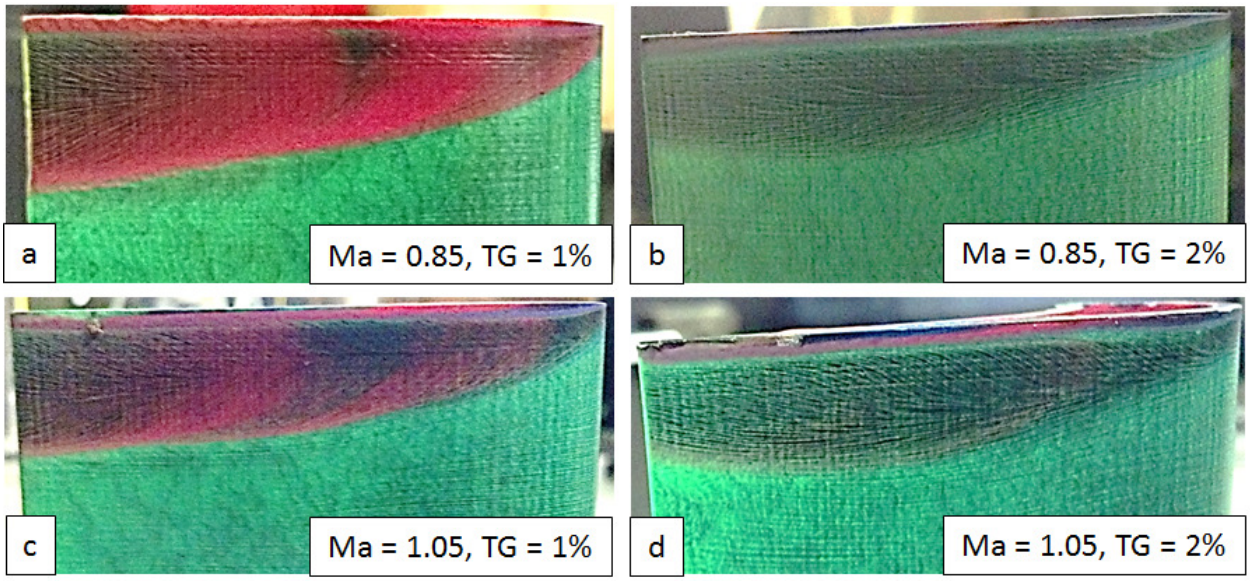

Figure 30. Squealer tip suction side oil flow visualization for Mach numbers of 0.85 and 1.05 and tip clearance gaps of 1% and 2% at a BR=1.0

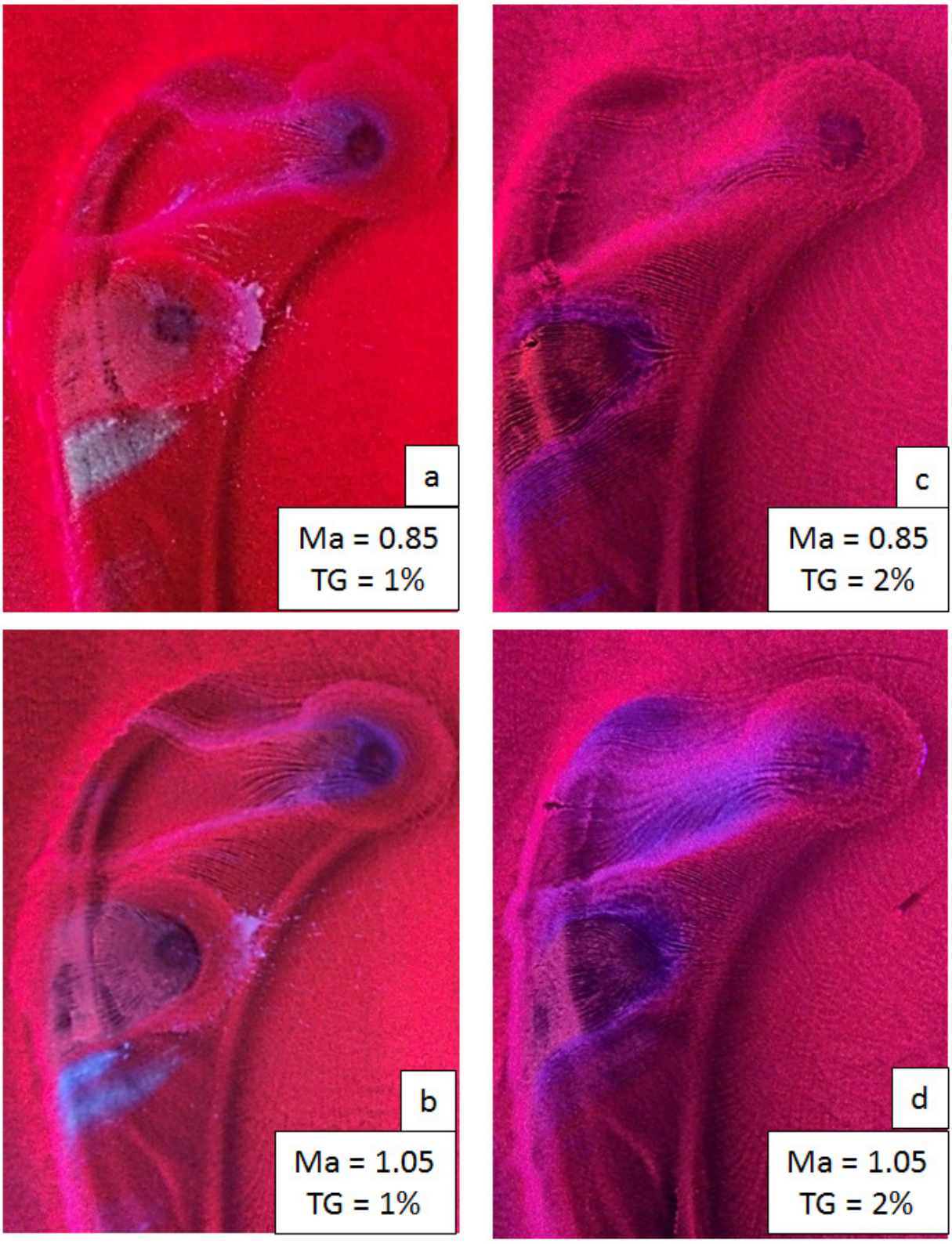

Figure 31. Squealer tip endwall oil flow visualization for Mach numbers of 0.85 and 1.05 and tip clearance gaps of 1% and 2%

Heat Transfer Results

Figures 32 through 36 show results of different distributions across the blade tip but have a common arrangement. The blades are oriented as they are in the test section, where incoming flow is horizontal and travels from left to right across the page. The left blade profile is the design condition at an exit Mach number of 0.85 and tip clearance gap of 1%. The right three blade profiles correspond to increases from the design condition of Mach number, 1.05, and tip clearance gap, 2%, respectively. Results for no purge flow blowing, blowing ratio of 0, are discussed first and are followed by purge flow blowing results, blowing ratio of 1.0. The purge hole to the right of the leading edge will be referred to as the first purge hole, while the mid-chord purge hole will be the second.

NO PURGE FLOW BLOWING, BLOWING RATIO = 0

Flat tip results are presented, in Figure 32, which are similar to those reported by Anto et al. [H.4]. ABS was used in the current set of results instead of Macor to improve upon the one-dimensional conduction assumption used in the calculation of heat flux. A linear regression data reduction technique was also used, which is similar to the technique described in this study, as opposed to the method documented by Ekkad et al. [H.5]. Their method approximates the incoming air temperature profile as a step change and does not adequately represent transient conditions. Similar trends are observed to those of Anto et al. [H.4] and are presented to provide a comparison between flat and squealer tip blades.

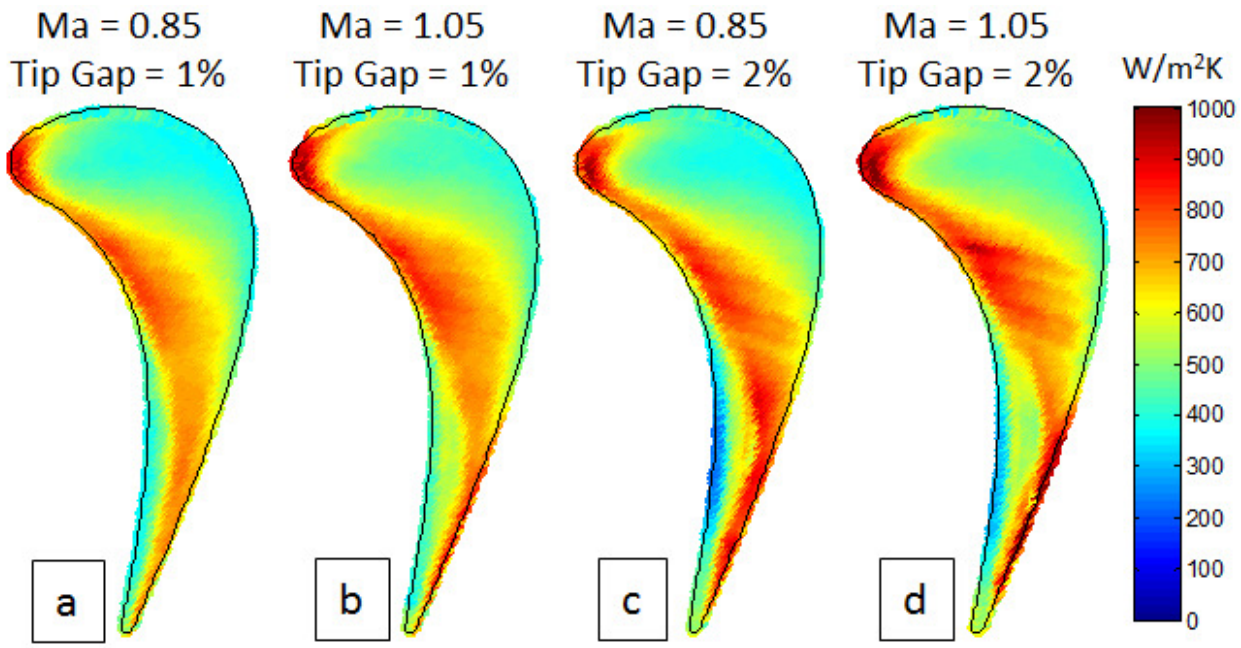

Figure 32. Heat transfer coefficient distributions of a flat tip blade of the same outer geometry as squealer tip blade of current study at different exit Mach numbers and tip clearance gaps

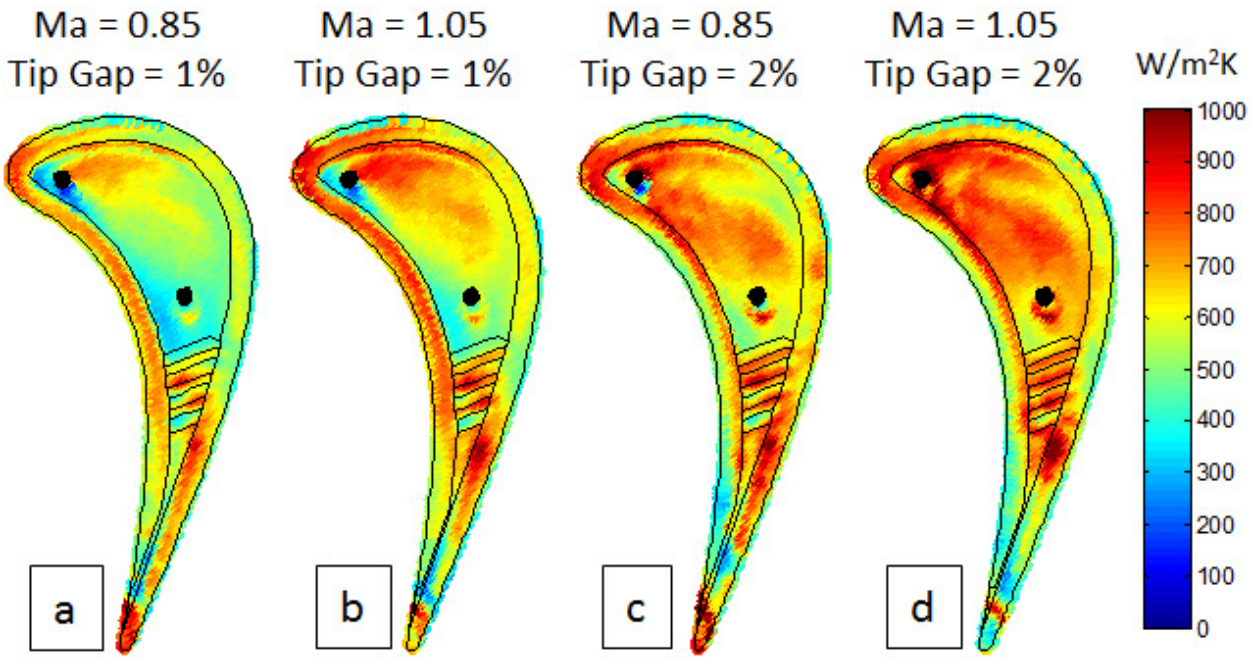

Figure 33. Heat transfer coefficient distributions of the squealer tip turbine blade at different exit Mach numbers and tip clearance gaps for a blowing ratio of 0

For both the flat and squealer tip blades, as Mach number and tip clearance gap increase, the heat transfer coefficient across the tip surface increases. These trends are in line with

literature; however, historically the average heat transfer coefficient across the whole tip should decrease as a result of the addition of a squealer tip, this trend is not observed in the current study. At the design condition, the average heat transfer coefficient is not appreciably different between the flat and squealer tips. For the off design conditions, the squealer tip heat transfer coefficient distributions are higher than those of the flat tip. This increase in heat transfer coefficient, as not observed in literature, is due to the presence of the support ribs. Reattaching mainstream flow in the upstream portion of the squealer cavity creates a high heat transfer coefficient region just behind the leading edge. The reattaching flow recirculates within the squealer tip and travels downstream where its path is obstructed by the ribs. An advantage of a typical squealer tip blade is to prevent reattachment of the hot mainstream flow towards the trailing edge with the development of a recirculation bubble. The support ribs do not allow the recirculation bubble downstream towards the trailing edge where its effect would be most profound. The reattachment region of the squealer tip blade near the leading edge also corresponds to the "sweet spot" of low heat transfer coefficient region observed by Anto et al. [H.4]. Therefore, the current squealer design increases heat transfer in low heat transfer flat tip areas and does not significantly reduce heat transfer in flat tip high heat transfer areas. However, for all three cases presented, the maximum heat transfer coefficient was observed on the flat tip blade. Ameri et al. [H.6] observed that the pressure side heat transfer coefficient distribution would be similar between flat and squealer tip blades, but portions of the cavity and suction side would be higher. This trend is observed in the current study for upstream portions of the blade not affected by the ribs.

For all four squealer tip cases, similar flow patterns are present. Reattachment and recirculation regions within the cavity are characterized by high and low heat transfer coefficients, respectively. As Mach number and tip clearance gap increase the reattachment regions get larger. Flow within the cavity travels downstream along the suction side rim while recirculating towards the pressure side. The support ribs assist this recirculation and direct the flow back upstream along the pressure side. High heat transfer regions around the second purge hole are due to flow being tripped turbulent by the purge hole itself. Downstream of the ribs is another reattachment region on the suction side rim where flow is tripped after crossing over the bleeder cavity. A clockwise, as viewed from the trailing edge, recirculation region develops in the bleeder cavity as a result of the mainstream flow crossing above. Bleeder cavity air is drawn

into the mainstream flow along the inside of the pressure side rim and directed upstream. This upstream flow is caused by a negative pressure gradient which forms when the lost bleeder cavity air is replaced by air supplied by the bleeder opening at the trailing edge. The bleeder air helps passively cool the last rib. At the trailing edge, where the bleeder cavity opens to the pressure side, a high heat transfer coefficient region forms. This region is in a location where the one-dimensional conduction assumption is suspect due to its proximity to both the pressure and suction side edges.

PURGE FLOW BLOWING, BLOWING RATIO = 1.0

Figures 34 and 35 correspond to the heat transfer coefficient and film cooling effectiveness distributions of squealer tip blade with purge flow blowing at a blowing ratio of 1.0. Regions in white are locations significantly affected by cooling air entering the test section before the mainstream flow and are therefore omitted. These omitted sections are believed to have low heat transfer coefficient and high film cooling effectiveness. Near the end of the testing schedule, air and small amounts of water leftover from oil-flow visualization tests began permeating through the surface of the tip in the trailing edge region. As a result the heat transfer coefficients are much lower and not representative of their actual values. For this reason, some trailing edge results are omitted. Edge points in the upstream suction side region are in error due to the cutting method and slight deflection in the blade towards the trailing edge during tunnel runs at high Mach numbers.

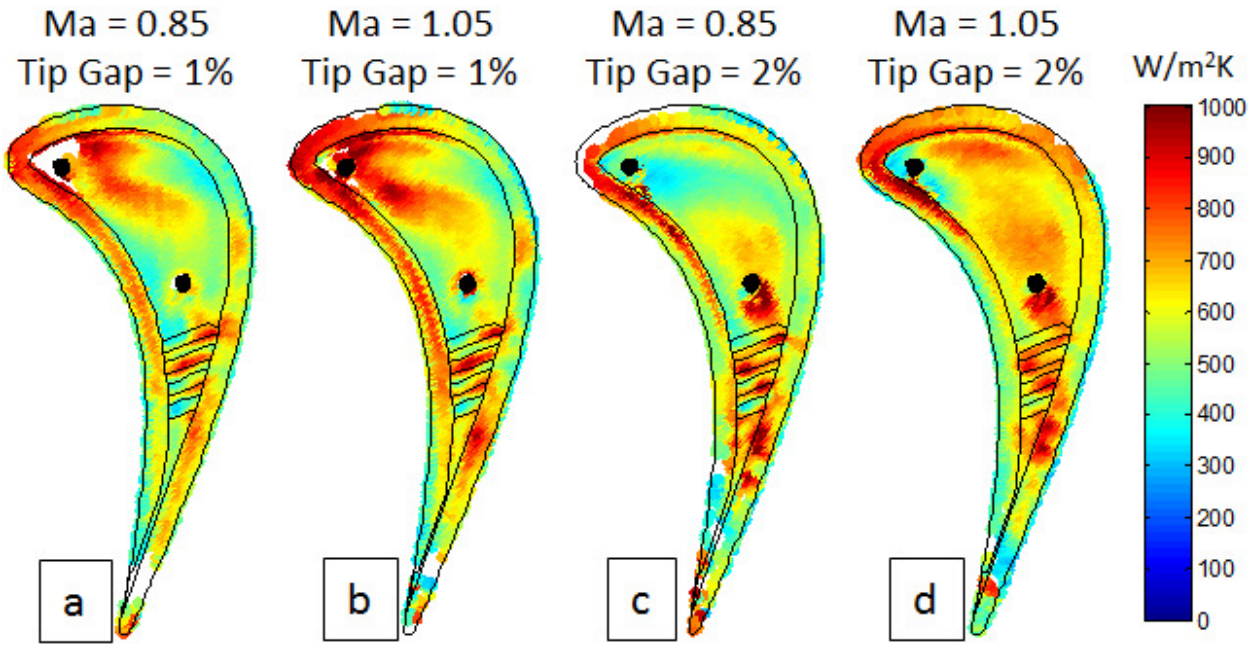

Figure 34. Heat transfer coefficient distributions of the squealer tip turbine blade at different exit Mach numbers and tip clearance gaps for a blowing ratio of 1.0

For increasing Mach number from 0.85 to 1.05 at a tip clearance gap of 1%, similar flow patterns appear. High heat transfer coefficient regions on the leading edge, in the cavity around the first purge hole and on the ribs, increase in size and magnitude with Mach number. High film cooling effectiveness regions appear around the purge holes and are directed towards the pressure side. With increasing Mach number, the film cooling effectiveness decreases.

Two reattachment regions appear in the cavity to the right of the leading edge. Impinging flow occurs where the mainstream flow reattaches and disperses outward from the reattachment location. A low heat transfer coefficient region lies in between the two reattachment regions where both impinging flows meet and a liftoff line appears. The flow from the liftoff line provides a second stream of cool air to mix with the mainstream flow and prevent a high heat transfer coefficient region from forming on the mid-cavity suction side rim. Just downstream, on the suction side rim is an area of high heat transfer coefficient which is an extension of the cavity reattachment region. The break in the reattachment region inside the suction side rim is caused by the cooler upstream flow traveling downstream and providing a buffer. Downstream of the leading edge a recirculation region where cooling air pools appears, as evidenced by the combination of low heat transfer coefficient and film cooling effectiveness. Some of the purge flow cooling air travels downstream along the inside of the pressure side rim, where its

effectiveness does not combine with that of the second purge hole. Flow just above of the second purge hole is directed downstream and towards the pressure side. A second recirculation region of purge flow cooling air develops as a result. The support ribs also help direct flow from the suction to pressure side; however, the presence of a rounded rib end leading to a concave point, on the right side of the first rib, creates a turbulent tripping point that has high heat transfer coefficient and low film cooling effectiveness. Downstream of the ribs, flow is similar to that of the no purge flow blowing cases. Bleeder cavity air travels upstream from the bleeder opening on the pressure side and helps keep the last rib's heat transfer coefficient low.

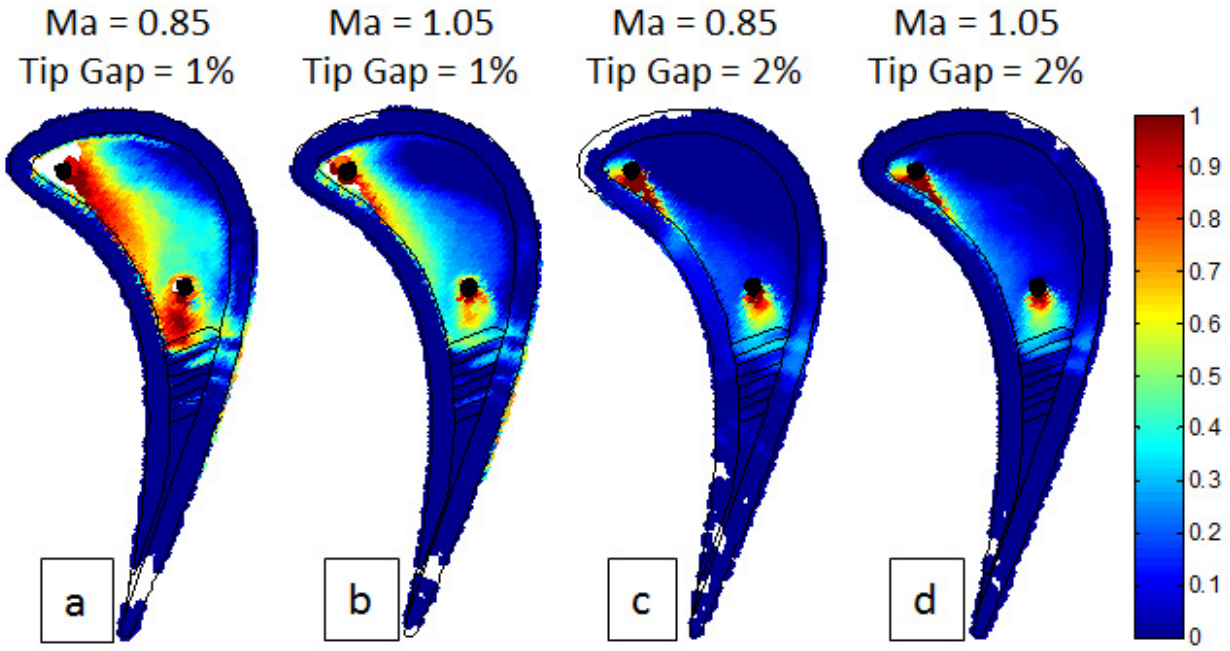

Figure 35. Film cooling effectiveness distributions of the squealer tip turbine blade at different exit Mach numbers and tip clearance gaps for a blowing ratio of 1.0

For increasing tip clearance gap from 1% to 2% of the scaled engine blade span at a Mach number of 0.85, slightly different flow patterns appear. The major contributor to the difference in flow patterns are the increase in leakage flow associated with an increased tip clearance gap. The heat transfer coefficient on the leading edge increases, especially along the pressure side, while the suction side is not significantly changed. Rib and bleeder cavity heat transfer coefficients increase significantly, while cavity heat transfer coefficients decrease. Film cooling effectiveness decreases significantly with tip clearance gap.

The two reattachment regions present in the 1% tip clearance gap cases are significantly diminished in size and magnitude. Increasing tip clearance gap diverts the lower reattachment

region and liftoff line downstream. Film cooling effectiveness around the first purge hole is directed towards the pressure side and is characteristic of a recirculation region. This recirculation region is much smaller than that observed in the 1% tip clearance gap case due to an increase of purge flow blowing air lost to the mainstream flow. While the first purge hole has less of a direct effect on tip heat transfer, its presence along with the downstream trend of an increased tip clearance gap diminishes the effect of the upper reattachment region. Near the second purge hole a complex flow region develops due to the close proximity of the reattachment region, purge hole and support ribs. The hot reattaching air mixes with that of the purge flow to create a high heat transfer coefficient and high film cooling effectiveness region, where turbulent flow is tripped by the proximity of the concave rib cavity. Recirculation around the second purge hole is not as strong as the 1% tip gap cases as evidenced by the suction side direction of the film cooling effectiveness distribution. Film cooling has an effect on the pressure side rim around mid-chord, where cooling air from the first purge hole replaces mainstream flow diverted by the second purge hole. High heat transfer coefficient regions on the pressure side of the second rib and suction side of the third rib are caused by reattachment of mainstream flow along a streamline. Upstream bleeder cavity flow is diminished and causes an increased heat transfer coefficient region on the suction side rim.

The fourth case, where Mach number is 1.05 and tip clearance gap is 2%, shows similar trends to that which have already been presented. An increase in tip clearance gap from 1% to 2% diverts the flow characteristics further downstream and reduces the effect purge flow blowing has on the blade surface. The overall magnitude of the heat transfer coefficient increases with Mach number.

Net heat flux reduction, NHFR, is a parameter used to evaluate the overall effect of the addition of purge flow blowing as compared with a no purge flow blowing case. Equation D.1 is used to calculate the net heat flux reduction where h_0 is the heat transfer coefficient of a no purge flow blowing case and ϕ is represented by Equation D.2. The value ϕ is estimated at 0.6, which is within the range of 0.5 and 0.7 used by Mehendale and Han [H-7]. Positive and negative values correspond to a decreases and increases in the net heat flux, respectively.

$$NHFR = 1 - \frac{q''}{q_0''} = 1 - \frac{h}{h_0}\left(1 - \frac{\eta}{\phi}\right) \tag{D.1}$$

$$\phi = \frac{T_w - T_r}{T_c - T_r} \tag{D.2}$$

Figure 36 shows the net heat flux reduction distributions for the three cases under examination. The net heat flux reduction is a measure of the overall effectiveness of the addition of purge flow blowing, where positive and negative values correspond to decreases and increases in tip heat transfer, respectively.

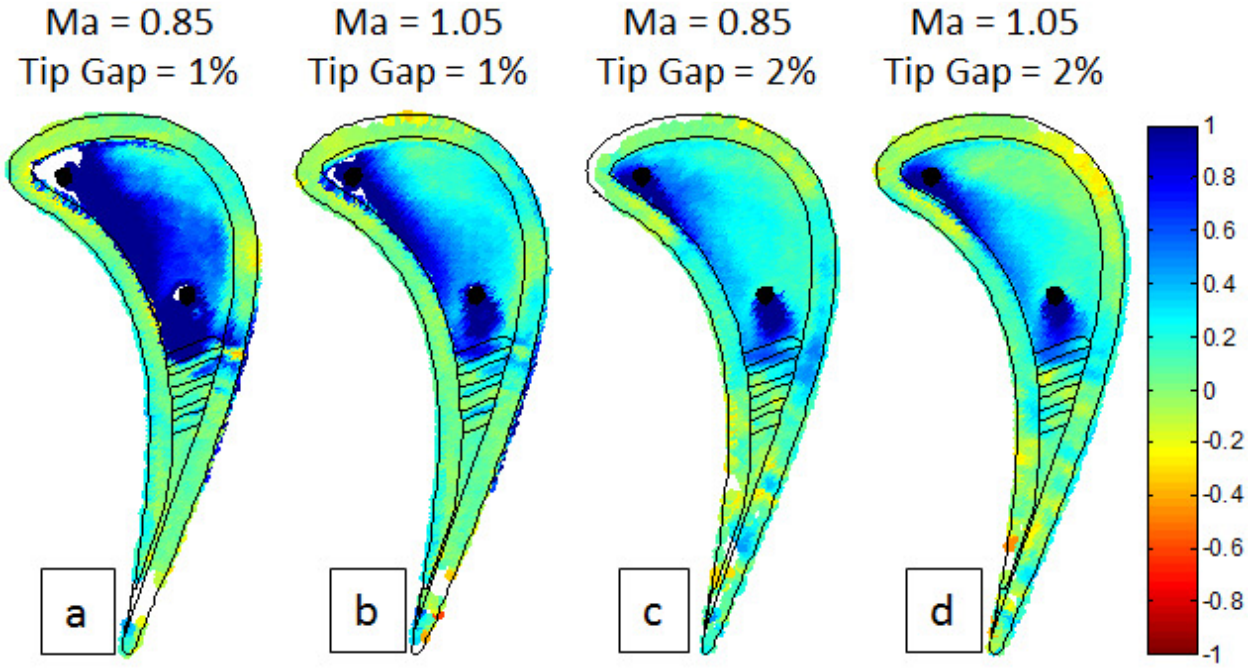

Figure 36. Net heat flux reduction distributions of the squealer tip turbine blade at different exit Mach numbers and tip clearance gaps

As Mach number and tip clearance gap increase the net heat flux reduction decreases. The first purge hole has the most significant impact on cavity heat transfer especially along the pressure side rim. The addition of purge flow blowing increases the heat transfer on the leading edge, on the suction side rim reattachment hotspot and at various locations downstream of the second purge hole. For the off design cases, purge flow blowing has little effect towards the suction side rim where heat transfer is dominated by reattaching flow.

Moderate improvements to heat transfer downstream of the second purge hole are present for the 1% tip clearance gap cases, suggesting leakage flow is lessened towards the trailing edge with the addition of blowing. Bleeder cavity heat transfer is moderately decreased. Adjacent to the first rib concave point on the suction side rim for the design case is an area of low net heat flux reduction. This area sees no film cooling effect due to the rib cavity immediately adjacent

and is downstream of a turbulent flow area. A similar band of no improved heat transfer is seen for the Mach 1.05 case.

For the 2% tip clearance gap case, streamline rib hotspots develop. Bleeder cavity flow is decreased and causes heat transfer to increase for the last rib. The suction side rim spot of high heat transfer is not present for the 2% tip clearance case.

COMPARISON OF FLAT AND SQUEALER TIP RESULTS

Figures 37 and 38 present the by region comparison of the average circumferential heat transfer coefficient and film cooling effectiveness for the flat and squealer tip blade cases at an exit Mach number of 1.05 and tip clearance gaps of 1% and 2%, respectively.

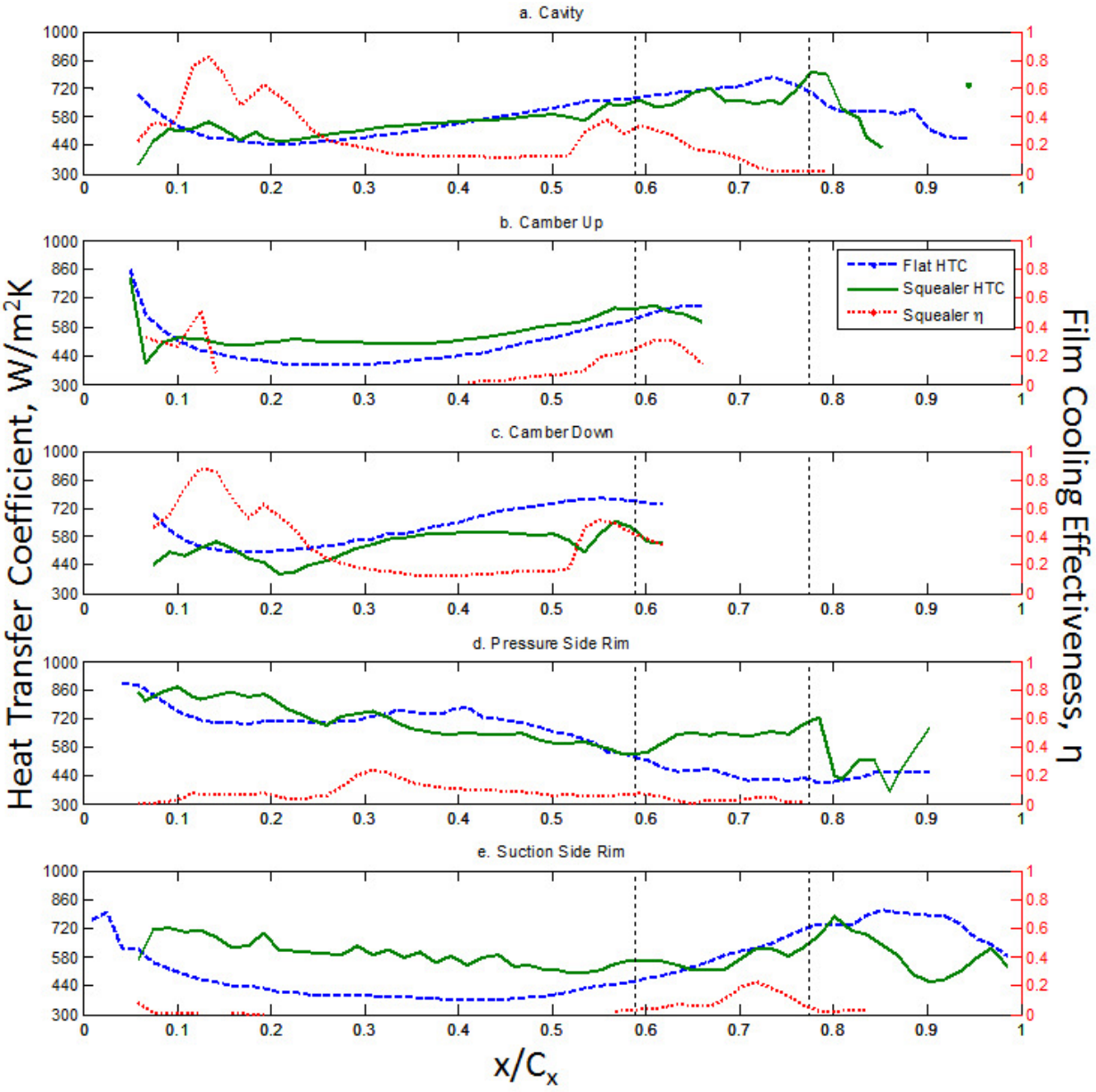

Figure 37. Circumferential averaged heat transfer coefficient and film cooling effectiveness results by region for flat and squealer tip blades at an exit Mach number of 1.05 and a tip clearance gap of 1%

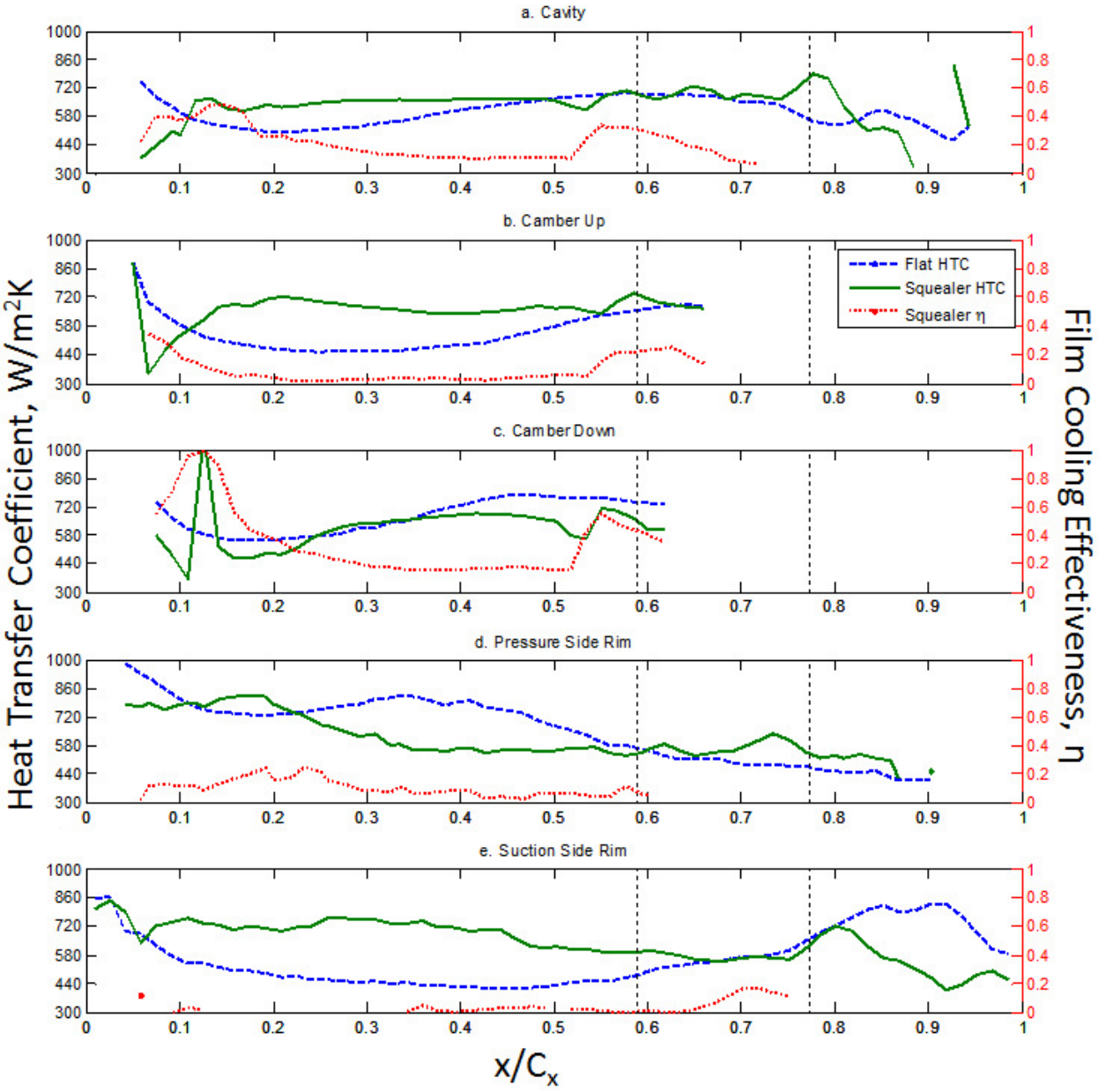

Figure 38. Circumferential averaged heat transfer coefficient and film cooling effectiveness results by region for flat and squealer tip blades at an exit Mach number of 1.05 and a tip clearance gap of 2%

Conclusions

The major findings of this experimental study are found below:

1. As Mach number increases, the average heat transfer coefficient increases, for all blade geometries, tip clearance gaps and blowing ratios.

2. Increasing tip clearance gap results in an increase in average heat transfer coefficient, for the no purge flow blowing cases.
3. For the no purge flow blowing cases, the largest heat transfer coefficient was observed on the leading edge. Flat tip maximum heat transfer coefficient was higher than that of the squealer tip for all no purge flow blowing cases.
4. Average heat transfer coefficient increases with the addition of a squealer tip, for the no purge flow blowing, off design cases, due to the presence of the mid-chord support ribs.
5. Squealer tip high heat transfer regions within the cavity are due to reattaching mainstream flow.
6. Heat transfer coefficient decreases with the addition of purge flow blowing.
7. Film cooling effectiveness decreases for increasing Mach number and tip clearance gap.
8. Film cooling effectiveness is directed towards the pressure side, which is a characteristic of recirculating flow.
9. The leading edge purge hole has a greater effect on film cooling effectiveness than the mid-chord purge hole.
10. Large improvements in cavity heat transfer are observed with the addition of purge flow blowing between the pressure side rim and camber line. Moderate improvements are observed between the camber line and suction side rim.
11. Bleeder cavity heat transfer is decreased moderately with the addition of purge flow blowing.

Appendix E: Accuracy of Finite-Difference Code

The finite-difference code used in this study was developed by Cress [H.2] and was based on a similar finite-difference code taught in Dr. Brian Vick's courses at Virginia Polytechnic Institute and State University. The code was originally developed to calculate the heat flux into the pressure and suction side of a turbine blade where two different materials were present. The finite-difference method was checked against the Laplace Transform Method being used at the time and found to produce the same results without spikes due to step changes in the inputs and oscillations as time increased. While the finite-difference method was an improvement over the Laplace Transform Method, the code used to carry out the finite-difference method was never checked for accuracy against an analytical solution. Figure 39 shows the temperature profile input into both the finite-difference code and Cook and Felderman [H.3] equation and Figure 40 shows the output of both methods. After the initial jump, the two results match to within 0.5% and it is within this time period that the data collected has an impact on the results. Therefore, either the finite-difference code or Cook and Felderman equation could be used. The finite-difference code is used because of its ability to model multiple materials and its calculation time is not significantly longer than using the Cook and Felderman equation.

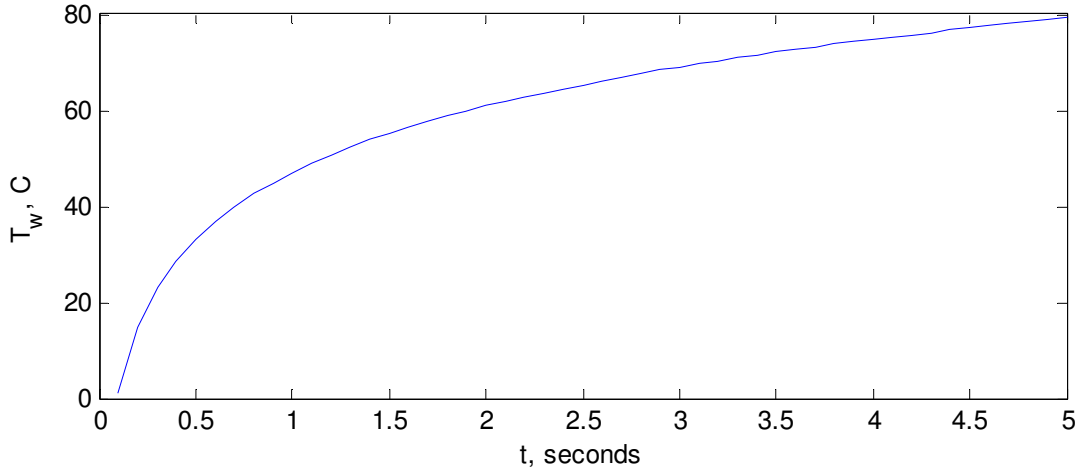

Figure 39. Temperature profile input into finite-difference code and Cook and Felderman equation

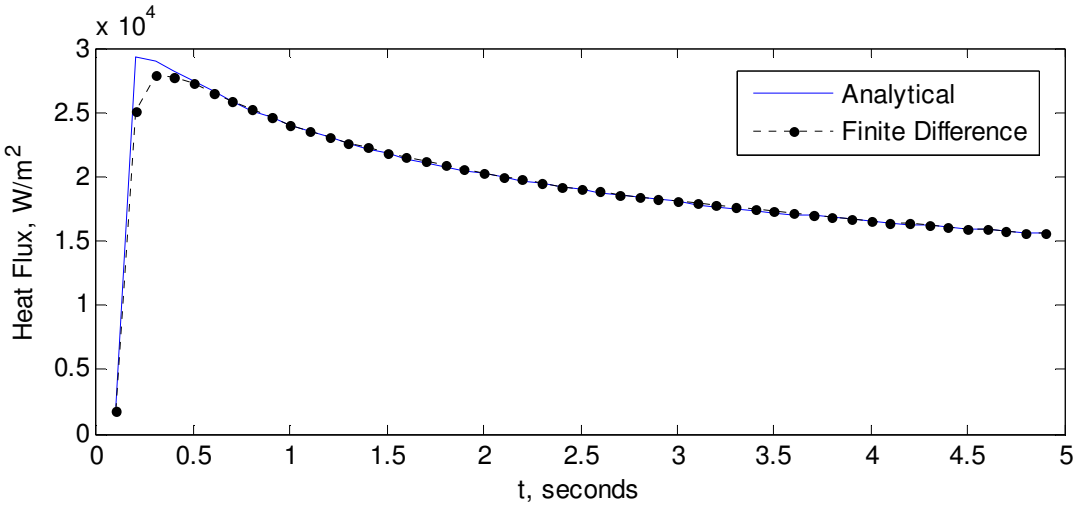

Figure 40. Output of finite-difference code and Cook and Felderman analytical solution

Appendix F: Material Properties Correction

Concerns have been raised about the accuracy of the material properties provided by the material supplier for the ABS P-430 3D printing plastic. Determining the material properties is outside the scope of this research, however, an investigation into the effect of an increase in the product of the relevant material properties, thermal conductivity, density and specific heat, has been done. The data reduction code was run for percent increases in the material properties up to about 200% and correlations were derived from these results. Given a percent increase in the product of the material properties an increase in the heat transfer coefficient based on Equation F.1 can be calculated. Film cooling effectiveness does not change appreciably with an increase in material properties. Figure 41 shows the results of a percent increase in heat transfer coefficient and film cooling effectiveness based on a percent increase in the thermal properties.

$$\mathrm{PD_{HTC}} = -0.0005 * \mathrm{PD_{k\rho C}}^2 + 0.46 * \mathrm{PD_{k\rho C}} + 0.31 \qquad \text{(F.1)}$$

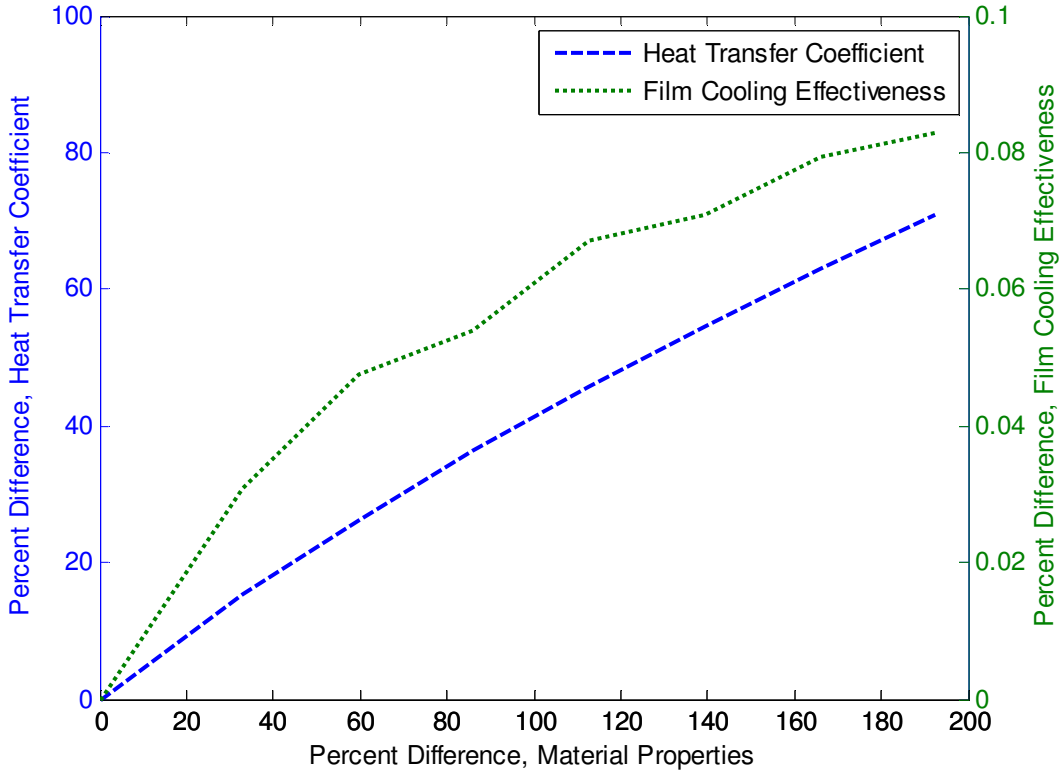

Figure 41. Correlation between a percent increase in the material property values and a percent increase in the heat transfer coefficient and film cooling effectiveness results presented in this study

Appendix G: Uncertainty Analysis

An uncertainty analysis described by Moffat [H.8] was performed during the heat transfer calculations of this study. Bias and precision errors were accounted for in this uncertainty analysis. Bias error is the uncertainty associated with the measurement setup and is caused by calibration, material property and data acquisition errors. Precision error is the uncertainty of reproducing a given experiment exactly and is caused by random error and unsteadiness. The bias and precision errors were calculated using the perturbation method, where the data reduction code was run repeatedly at the minimum and maximum values of the various calibration and measurement accuracies and a root-sum-square method of the difference between the accuracy range and reported values was used to calculate the total bias and precision uncertainties.

Equations G.1 and G.2 were used to calculate the precision and bias uncertainties in the reported results, respectively, where R is the result in question. Tables G-1 and G-2 show the calculation of the precision and bias uncertainties for the heat transfer coefficient and film cooling effectiveness, respectively. Combining the precision and bias errors using the root-sum-square method, the total uncertainty within the heat transfer coefficient and film cooling effectiveness calculations are 14.14% and 0.102, respectively.

$$Precision = \sqrt{(R - R_{T_w})^2 + (R - R_{T_c})^2 + (R - R_{T_\infty})^2} \quad \text{(G.1)}$$

$$Bias = \sqrt{(R - R_k)^2 + (R - R_{C_p})^2 + (R - R_\rho)^2} \quad \text{(G.2)}$$

Table 1. Calculation of the precision, bias and total uncertainty within the heat transfer coefficient measurements

	X_i	Units	dX_i	$d(H_{Xi})$	
				W/m^2K	%
Precision	T_w	°C	2	66.46	9.35
	T_c	°C	2.3	10.43	1.44
	T_m	°C	2.3	50.40	7.30
	Total Precision Uncertainty			84.06	11.95
Bias	k	W/mK	0.009	14.97	2.52
	ρ	kg/m^3	207.5	2.79	0.47
	C_p	J/kgK	10	42.35	7.12
	Total Bias Uncertainty			45.00	7.56
Total Uncertainty				95.35	14.14

Table 2. Calculation of the precision, bias and total uncertainty within the film cooling effectiveness measurements

	X_i	Units	dX_i	$d(\eta_{Xi})$
				Unit less
Precision	T_w	°C	2	0.0760
	T_c	°C	2.3	0.0154
	T_m	°C	2.3	0.0445
	Total Precision Uncertainty			0.0894
Bias	k	W/mK	0.009	0.0163
	ρ	kg/m^3	207.5	0.0030
	C_p	J/kgK	10	0.0463
	Total Bias Uncertainty			0.0492
Total Uncertainty				0.1021

Appendix H: Appendix References

[H.1] Nasir, S., Carullo, J.S., Ng, W.F., Thole, K.A., Wu, H., Zhang, L.J., and Moon, H.K., 2009, "Effects of Large Scale High Freestream Turbulence, and Exit Reynolds Number on Turbine Vane Heat Transfer in a Transonic Cascade," ASME J. Turbomach., 131, 021021.

[H.2] Cress, R. D., 2006, "Turbine Blade Heat Transfer Measurements in a Transonic Flow Using Thin film Gages," *Master's Thesis, Virginia Polytechnic Institute and State University.*

[H.3] Cook, W. J., and E. M. Felderman. "Reduction of Data from Thin-film Heat-transfer Gages - A Concise Numerical Technique." *AIAA Journal* 4.3 (1966): 561-62. Print.

[H.4] K. Anto, S. Xue and W.F. Ng, L.J. Zhang and H.K. Moon, "Effects of Tip Clearance Gap and Exit Mach Number on Turbine Blade Tip and Near-Tip Heat Transfer," Proceedings of ASME Turbo Expo GT2013-94345.

[H.5] Ekkad, S. V., Ou, S., and Rivir, R. B., 2004, "A Transient Infrared Thermography Method for Simultaneous Film Cooling Effectiveness and Heat Transfer Coefficient Measurements From a Single Test," *ASME J. Turbomach*., 126, pp. 546–553.

[H.6] Ameri, A. A., E. Steinthorsson, and D. L. Rigby. "Effect of Squealer Tip on Rotor Heat Transfer and Efficiency." *Journal of Turbomachinery* 120.4 (1998): 753-59. Print.

[H.7] Mehendale, A. B., Han, J. C., 1993, "Reynolds number Effect on Leading Edge Film Effectiveness and Heat Transfer Coefficient," *Int. J. Heat and Mass Transfer*, 36, pp. 3723-3730.

[H.8] Vick, B., "Finite Difference Method", Class Notes, Virginia Tech Mechanical Engineering Department.

[H.9] Moffat, R. J., 1988, "Describing Uncertainties in Experimental Results," *Exp. Thermal and Fluid Science*, 1988, pp. 3-17.